Journal of the Mechanics and Physics of Solids 123 (2019) 61–79

Contents lists available at ScienceDirect

Journal of the Mechanics and Physics of Solids

journal homepage: www.elsevier.com/locate/jmps

Bifurcation analysis of twisted liquid crystal bilayers

K. Danas [a,*], D. Mukherjee [a], K. Haldar [b], N. Triantafyllidis [a,c]

[a] LMS, C.N.R.S., École Polytechnique, Palaiseau 91128, France
[b] Department of Aerospace Engineering, Indian Institute of Technology Bombay, Mumbai 400076, India
[c] Aerospace Engineering Department & Mechanical Engineering Department (emeritus), The University of Michigan, Ann Arbor, MI 48109-2140, USA

ARTICLE INFO

Article history:
Received 7 July 2018
Revised 8 September 2018
Accepted 8 September 2018
Available online 12 September 2018

Keywords:
Liquid crystal
Bifurcation
Finite elements
Nematic

ABSTRACT

This work presents a general methodology to analyze three-dimensional Freedericksz transitions in twisted-nematic liquid crystal (LC) bilayers. Using two equivalent coupled electromechanical variational formulations, the problem is treated as a bifurcation instability triggered by an externally applied electric field. Specifically, we consider LC bilayer materials anchored between two bounding plates and subjected to an electric field across the bilayer thickness. The plates are also twisted by an overall angle leading to different orientations of the directors in each layer. We first evaluate the corresponding ground state of the director field, and subsequently, we analyze the bifurcation problem by using a combined analytical-numerical method leading to a one-dimensional finite element discretization of the resulting stiffness matrix of the system. An analytical solution for the zero-twist bilayer is also obtained. The developed methodology is used to study the effect of the volume fraction of the constituents forming the bilayer upon the resulting critical electric field and corresponding eigenmodes. We find that by assembling a relatively thin 5CB layer with a thicker 7E layer, one can obtain periodic Freedericksz transitions (i.e. local modes) even for a zero-twist LC bilayer. We also show that when a 5CB material is assembled together with another electrically similar LC, such as a PCH12, the combined LC bilayer can exhibit an even lower Freedericksz transition than a LC of the same thickness consisting of any of the two constituents alone.

1. Introduction

Liquid crystals (LCs) are materials made of elongated rod-like molecules, called directors, that have a preferred average orientation thus resulting to an overall anisotropic behavior. Due to their response to external stimuli (electric, magnetic or thermal fields), LCs are extensively used in electronic devices and particularly in optical displays. In simple terms, a liquid crystal display (LCD) is essentially a thin layer of an LC material, anchored between two bounding plates, typically, made of transparent polymer or glass and optically polarized in different directions. In the absence of a transverse (i.e., normal to the bounding plates) electric (or magnetic) field, all the directors (nematic or cholesteric) lie in the same plane as that of the bounding plates. In most cases, these directors are all aligned at a given in-plane direction (e.g. nematic LC) or form helices across the thickness (e.g. twisted-nematic, cholesteric). In the absence of an external electric field, these configurations allow polarized light to pass through the two end plates. When an applied transverse electric field exceeds

* Corresponding author.
E-mail addresses: konstantinos.danas@polytechnique.edu (K. Danas), nicolas.triantafyllidis@polytechnique.edu (N. Triantafyllidis).

https://doi.org/10.1016/j.jmps.2018.09.008
0022-5096/

a critical value, the directors suddenly rotate out-of-plane to align with the applied transverse field. This changes the path followed by the polarized light resulting to the blocking of its transmission through the end plates. This phenomenon can be modeled as a bifurcation of an appropriate boundary value problem and is called the *Freedericksz transition* (Fréedericksz and Repiewa, 1927). Such a *switching* in the optical properties has been extensively exploited over the last forty years and led to the spectacular development of the industry of LC displays and color-light screens (Gray and Kelly, 1999; Kirsch and Bremer, 2000; Wysocki et al., 1969).

A more efficient way of optical switching may be obtained by use of twisted nematic displays (TNDs) (Gray and Kelly, 1999; Kirsch and Bremer, 2000). TNDs are obtained when a pre-twist is applied between the parallel plates that anchor the nematic LC phase (Schadt and Helfrich, 1971). Freedericksz transition in TNDs requires the application of an electric field whose critical value depends on the pre-twist (Leslie, 1970; Sfyris et al., 2016). The resulting distorted patterns in such post-bifurcated TN layers depend on their mechanical and electric (or magnetic) properties (Leslie, 1970).

In turn, a large number of studies have been devoted to the theoretical continuum description of LCs. In particular, a continuum model for the description of LCs in terms of a free energy density was first introduced by Oseen (1933) and Frank (1958), while the theory to model the time-dependent behavior was proposed later by Ericksen (1962) and Leslie (1968). For a complete three-dimensional, quasi-static framework for TN phases the reader is referred to the books of Virga (1994) (variational approach) and Stewart (2004) (direct approach). More recently, Pampolini and Triantafyllidis (2018) have developed a variational framework for nematic elastomers, i.e., LCs that can undergo finite deformations. In all these works, the Frank-Oseen (FO) energy has served as a basis for the description of the continuum framework. More specifically, the bulk FO energy consists of three mechanical contributions, namely, the splay, twist and bending energy of the material. This description is sufficient for modeling strongly anchored LC layers (Kini, 1987; Pampolini and Triantafyllidis, 2018; Sfyris et al., 2016). On the other hand, additional energetic contributions due to surface tension may become significant if one is interested to model the LC free surfaces (Lavrentovich and Pergamenshchik, 1996) or *weakly* anchored LC layers (Rosso et al., 2004; Sugimura et al., 1995).

As already mentioned in the beginning of this introduction, the main mechanism of operation in LCs is the Freedericksz transition. When the resulting transition (bifurcation) pattern depends only on the thickness coordinate, one has a *global* mode of instability (Blinov, 1979; Sfyris et al., 2016). By contrast, Lonberg and Meyer (1985) have observed spatially periodic twist-splay patterns in nematic liquid crystals, which correspond to a *local* mode of instability (Sfyris et al., 2016). In particular, such periodic distortions arise in a nematic LC whenever the ratio of its splay and twist stiffness exceeds a specific threshold. Such periodic distortions have also been observed in TN LC layers when the pre-twist exceeds a critical twist angle (Sfyris et al., 2016).

In particular, the effect of the pre-twist upon the critical electric field has been examined by Leslie (1970) analytically and validated experimentally by Gerritsma et al. (1971) and Karat and Madhusudana (1977). More recently, Atherton and Sambles (2006) investigated similar post-instability periodic pattern formations in nematic-homeotropic LC layers. Instabilities in solid LC elastomers have been observed, on the other hand, by Bladon et al. (1993) and Warner and Terentjev (2003), while recently, Sonnet and Virga (2017) have observed curvature-dependent periodic patterns in the post-bifurcation regime of LC polymers (Sonnet and Virga, 2017).

The periodic patterning of thin nematic layers, which is one of the limiting cases in the present study, has been observed in a number of experiments (Lavrentovich and Pergamenshchik, 1990). In such studies, thin layers of nematic phases are typically anchored to a soft polymer or a liquid substrate. Theoretical investigations show that the surface energy of the free thin film of a nematic layer is much higher when compared to that of the substrate. Consequently, the thin LC layer buckles in order to achieve a greater surface area, resulting in a periodic pattern, which is also termed as the *spontaneous* Freedericksz transition (Barbero and Durand, 1987; Kaznacheev and Sonin, 1983). This spontaneous nematic to periodic transition of a nematic film depends as expected on its thickness (Alexe-Ionescu et al., 2002; Sparavigna et al., 1994) and thus *only* takes place below a critical thickness of the nematic layer (Sparavigna et al., 1994). In this context, Sprang and Aartsen (1985) and Sugimura et al. (1998) have shown that the anchoring strength of the thin nematic layers on a substrate depends on the surface tension of the nematic film as well as on the surface roughness of the interface. Interestingly, reverse switching of surface roughness and wrinkling has been observed by Liu et al. (2015) in a self-organized polydomain liquid crystal coating. More recent experiments with nematic phase-polymer bilayers show complex surface patterns and shape changes including wrinkling, helical twisting and folding (Agrawal et al., 2014; Boothby and Ware, 2017; Liu et al., 2017). These recent observations reveal the complex interactions of nematic layers with soft substrates and call for an in depth investigation of instabilities in LC multi-layer assemblages.

Scope of the study. In this view, our study focuses on the theoretical investigation of the stability of TN bilayers made of two distinct LC phases with different mechanical and dielectric properties. More specifically, in an effort to provide a general methodology to analyze three-dimensional Freedericksz transitions as well as to carry out an insightful analysis of the Freedericksz transition in TN bilayers, we propose a variational framework for multilayer TN composites, extending the work of Stewart (2004) and Sfyris et al. (2016) for the single phase TN layers. Two formulations, one using a vector potential and the other a scalar potential, are discussed in detail and are shown to be exactly equivalent by means of a non-trivial boundary value problem (BVP). The resulting BVP along with the strong anchoring and the interface conditions is solved to obtain the bifurcation values of the applied electric fields as well as the corresponding patterns (local and global modes). The presence of an interface in-between the two layers requires the definition of a new ground state for each layer for non-zero twist. This is achieved by introducing a reduced potential energy for the director field prior to the application of

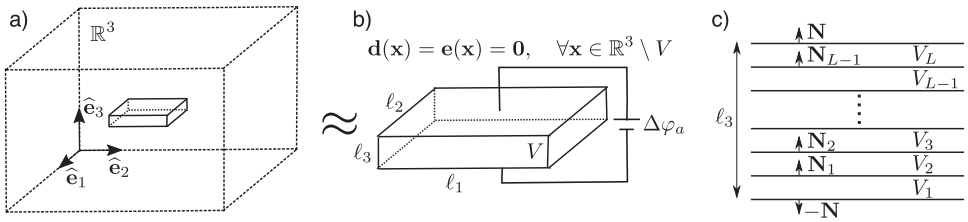

Fig. 1. (a) Geometry of the $\mathbb{R}^3$ dimensional problem depicting the LC device. (b) The LC device of volume V and its dimensions ℓ_1, ℓ_2 and ℓ_3. (c) A paradigm of a layered LC device comprising $r = 1, L$ phases occupying volumes V_r.

an electric field and is general for any multi-layer LC with any number of interfaces. The reduced potential allows to recover in a straightforward manner the ground state of a single LC layer reported in the literature. The bifurcation analysis of the present BVP is achieved via a combined analytical-numerical method (Sfyris et al., 2016) which leads to an one-dimensional finite-element discretization along the thickness of the bilayer. An analytical bifurcation analysis is also performed for the special case of purely nematic (no-twist) bilayers. A single layer made of a 5CB material, which has been investigated in detail by Sfyris et al. (2016), is now anchored to another LC layer leading to periodic patterns even in the simple zero-twist case. Moreover, we show that when the 5CB is assembled together with another LC that exhibits similar values of the critical electric field (such as PCH12), the resulting LC bilayer can lead to an even lower Freedericksz transition electric field than any of the constituents alone.

The present work is organized as follows. Section 2 describes two equivalent versions of the general variational framework for multi-layered LC materials. This is followed by the definition of the LC bilayer geometry and the corresponding expressions for the FO energy in Section 3. The finite-element framework for the bifurcation analysis of TN bilayers is then discussed in Section 4, followed by an analytical solution for the special case of zero-twist (nematic LC) in Section 5. The results in Section 6 consist of two parts. The first part, in Section 6.1, shows the critical electric field and the critical wavenumbers for the Freedericksz transition in a TN bilayer made of arbitrary volume fractions of 5CB and 7E LC materials. The second part, in Section 6.2, investigates the variation of the critical electric field and the corresponding wavenumbers obtained by assembling bilayers made of a 5CB layer and four other LC phases. We conclude the study with general remarks and suggestions for future work in Section 7. Finally, in the electronic Supplemental Material (SM), we provide additional algebraic details on the analytical solution.

2. Definition of the potential energy

In this section, we present the variational formulations used to analyze a LC boundary value problem (BVP). The discussion that follows is based on the sketch of Fig. 1. Our LC is an infinite multilayer of thickness ℓ_3 and occupies a volume V which comprises $r = 1, L$ different phases occupying volumes V_r, respectively (see Fig. 1c for a multi-layer example). The LC materials are regarded in the present work as nematic and/or TN described by a free energy density w_d (or w_e). This energy can be split into a mechanical free energy density that is a function of the orientation of the director vector $\mathbf{n}(\mathbf{x})$ and its gradient $\nabla\mathbf{n}(\mathbf{x})$ (but not of the deformation gradient), and an electrical free energy that depends on $\mathbf{n}(\mathbf{x})$ and the electric displacement $\mathbf{d}(\mathbf{x})$ (or the electric field $\mathbf{e}(\mathbf{x})$). Specific definitions of these energies are provided in Section 3. Here, $\mathbf{x}$ denotes the position vector in the current configuration, which coincides with the reference configuration since there is no dependence on the deformation gradient. Henceforth, the $\mathbf{x}$ argument will be dropped for simplicity of notation whenever considered unnecessary.

Specifically, we will present two different but equivalent variational formulations: a vector potential formulation for the electric displacement $\mathbf{d}$ (leading to a Neumann BVP for the electric part) and a scalar potential formulation for the electric field $\mathbf{e}$ (leading to a Dirichlet BVP for the electric part). The first formulation is more suitable for numerical calculations, while the second leads to an easier analytical solution for the no-twist case.

2.1. A vector potential formulation for the electric displacement

The interest in the present work is the investigation of the three dimensional bifurcation of LCs, and thus, it is convenient to formulate an energy minimization problem. This will allow us to numerically calculate the critical electric field at the onset of bifurcation as the minimum eigenvalue of the incremental stiffness (or Hessian) matrix for the corresponding discretized potential energy. In this regard, for the BVP sketched in Fig. 1a, we define the potential energy as

$$\mathcal{P}_d^{\mathbb{R}^3}(\mathbf{n}, \nabla\mathbf{n}, \mathbf{d}) = \inf_{\mathbf{n}\in\mathcal{S}} \inf_{\mathbf{d}\in\mathcal{D}} \left\{ \int_V w_d\big(\mathbf{x}, \mathbf{n}, \nabla\mathbf{n}, \mathbf{d}\big) dV + \int_{\mathbb{R}^3\setminus V} \frac{1}{2\,\varepsilon_0} \mathbf{d}\cdot\mathbf{d}\, dV + \int_{\partial V} (\mathbf{e}_a \times \boldsymbol{\alpha})\cdot\mathbf{N}\, dS \right\}, \tag{2.1}$$

where $\varepsilon_0 \simeq 8.854 \cdot 10^{-12}\mathrm{F}\cdot\mathrm{m}^{-1}$ denotes the electric permittivity of free space, $\mathbf{e}_a$ is the applied electric field on the boundary of the LC material and $\mathbf{N}$ denotes the normal to the boundary. Note that in the above-defined potential energy, we neglect mechanical body forces and free charges. We proceed further by introducing the approximation sketched in Fig. 1b.

Therein, we take into account first that the electric potential difference $\Delta\varphi_a$ is directly applied between the upper and lower surfaces of the LC (see Fig. 1b). This leads to the electric field being identically zero outside the LC in the direction x_3 and equal to

$$\mathbf{e}_a = \frac{\Delta\varphi_a}{\ell_3}\mathbf{e}_3 \tag{2.2}$$

on the boundary ∂V. It is worth noting here that since the independent variable used in the potential energy in (2.1) is the electric displacement $\mathbf{d}$ (or equivalently the vector potential $\boldsymbol{\alpha}$), the application of the conjugate electric field $\mathbf{e}_a$ on the boundary of the LC makes it a Neumann BVP (see last integral term in (2.1)).

Secondly, we note that in a LC device, the corresponding dimension in the x_3 direction is smaller than in the other two. These considerations allow us to model only the LC system neglecting the surrounding air and redefining the volume as $V = \mathbb{R}^2 \times [0, \ell_3]$. In view of this, the potential energy (2.1) can be simplified to

$$\mathcal{P}_d(\mathbf{n}, \nabla\mathbf{n}, \boldsymbol{\alpha}) = \inf_{\mathbf{n}\in\mathcal{S}} \inf_{\boldsymbol{\alpha}\in\mathcal{D}} \left\{ \int_V w_d(\mathbf{x}, \mathbf{n}, \nabla\mathbf{n}, \mathbf{d})\mathrm{d}V + \int_{\partial V} (\mathbf{e}_a \times \boldsymbol{\alpha}) \cdot \mathbf{N}\,\mathrm{d}S \right\}, \tag{2.3}$$

with the admissible sets for the director field $\mathbf{n}$ and the electric displacement vector potential $\boldsymbol{\alpha}$ defined by

$$\mathcal{S} \equiv \left\{ \mathbf{n}(\mathbf{x}) : \mathbf{n}(\mathbf{x}) \cdot \mathbf{n}(\mathbf{x}) = 1, \ \ \forall \mathbf{x} \in V, \mathbf{n}(\mathbf{x}) = \mathbf{n}_{\partial V}, \ \ \forall \mathbf{x} \in \partial V \right\} \tag{2.4}$$

and

$$\mathcal{D} \equiv \left\{ \mathbf{d}(\mathbf{x}) : \nabla \cdot \mathbf{d}(\mathbf{x}) = 0, \ \ \mathbf{d}(\mathbf{x}) = \nabla \times \boldsymbol{\alpha}(\mathbf{x}), \quad \nabla \cdot \boldsymbol{\alpha}(\mathbf{x}) = 0 \quad \forall \mathbf{x} \in V \right\}. \tag{2.5}$$

Here, the introduction of $\boldsymbol{\alpha}$ ensures that $\mathbf{d}$ is divergence free. In addition, the constraint $\nabla \cdot \boldsymbol{\alpha} = 0$ corresponds to the well-known Coulomb gauge and leads to a uniquely defined vector potential $\boldsymbol{\alpha}$ (Bíró and Preis, 1984; Stark et al., 2015). By extremizing the potential energy $\mathcal{P}_d$ in (2.3) with respect to $\mathbf{n}$ and $\boldsymbol{\alpha}$, one obtains the Euler-Lagrange field equations, i.e. the equilibrium, the Faraday equations and the corresponding jump conditions at internal interfaces

$$(\mathcal{P}_d)_{,\mathbf{n}}\delta\mathbf{n} = 0 \ \ \Rightarrow \ \ \nabla \cdot \frac{\partial w_d}{\partial \nabla\mathbf{n}} - \frac{\partial w_d}{\partial \mathbf{n}} = \mathbf{0}, \quad \forall \mathbf{x} \in V, \qquad \left[\!\left[\frac{\partial w_d}{\partial \nabla\mathbf{n}} \right]\!\right]\mathbf{N}_i = \mathbf{0}, \quad [\![\mathbf{n}]\!] = 0, \quad \forall \mathbf{x} \in \partial V_r, \tag{2.6}$$

$$(\mathcal{P}_d)_{,\boldsymbol{\alpha}}\delta\boldsymbol{\alpha} = 0 \ \ \Rightarrow \ \ \nabla \times \mathbf{e} = \mathbf{0}, \quad \mathbf{e} = \frac{\partial w_d}{\partial \mathbf{d}}, \quad \forall \mathbf{x} \in V, \quad \mathbf{N}_i \times [\![\mathbf{e}]\!] = 0, \quad \forall \mathbf{x} \in \partial V_r, \tag{2.7}$$

as well as the Dirichlet on $\mathbf{n}$ and Neumann on $\mathbf{e}$ boundary conditions

$$\mathbf{n} = \mathbf{n}_{\partial V}, \qquad \mathbf{N} \times \mathbf{e} = \mathbf{N} \times \mathbf{e}_a, \quad \forall \mathbf{x} \in \partial V. \tag{2.8}$$

In the very last equation, we have used the fact that $\mathbf{e} = \mathbf{0}$ outside the V (see Fig. 1b). Note further that to the field equations (2.6) and (2.7), one needs to add the constraints described in (2.4) and (2.5). This is described in detail in the next section.

In the present study, the notation $\mathbf{N}_i$ is used to describe the normal at an interface between two phases occupying volumes V_r and V_{r+1} (with $r = 1, L$ phases), while its positive direction is chosen to be from phase i to phase $i+1$, i.e., $\mathbf{N}_i = \mathbf{N}_{i\to i+1}$, as sketched in the multi-layer example in Fig. 1c.

2.2. An alternative potential energy using the scalar electric potential

In Section 5, we propose an analytical solution to the problem for the special case of zero twist. For this case it is more convenient to use an alternative but equivalent definition of the potential energy, denoted as $\mathcal{P}_e$, which is written in terms of the electric field $\mathbf{e}$ (or the scalar potential φ). For that, one needs to define first the partial Legendre-Fenchel transforms of the energies w_d and w_e (Bustamante et al., 2009) with respect to $\mathbf{d}$ and $\mathbf{e}$, to obtain

$$w_e(\mathbf{n}, \nabla\mathbf{n}, \mathbf{e}) = \underset{\mathbf{d}}{inf}[-\mathbf{e}\cdot\mathbf{d} + w_d(\mathbf{n}, \nabla\mathbf{n}, \mathbf{d})] \quad \text{and} \quad w_d(\mathbf{n}, \nabla\mathbf{n}, \mathbf{d}) = \underset{\mathbf{e}}{sup}[\mathbf{e}\cdot\mathbf{d} + w_e(\mathbf{n}, \nabla\mathbf{n}, \mathbf{e})]. \tag{2.9}$$

The above transformation leads to a unique result for strictly convex energy function, which will be the case in the present study (see definitions for w_e and w_d in Section 3.1). Using next the transformation $(2.9)_1$, one can readily define the equivalent potential energy in terms of $\mathbf{e}$ (or the scalar potential φ) as

$$\mathcal{P}_e(\mathbf{n}, \nabla\mathbf{n}, \varphi) = \inf_{\mathbf{n}\in\mathcal{S}} \sup_{\varphi\in\mathcal{E}} \int_V w_e(\mathbf{x}, \mathbf{n}, \nabla\mathbf{n}, \mathbf{e})\mathrm{d}V. \tag{2.10}$$

Here, $\mathcal{S}$ is defined in (2.4), whereas the admissible set $\mathcal{E}$ is given by

$$\mathcal{E} = \left\{ \mathbf{e}(\mathbf{x}) : \nabla \times \mathbf{e}(\mathbf{x}) = 0, \ \ \mathbf{e}(\mathbf{x}) = -\nabla\varphi(\mathbf{x}), \ \ \forall \mathbf{x} \in V, \qquad \varphi(\mathbf{x}) = \mathbf{e}_a \cdot \mathbf{x}, \ \ \forall \mathbf{x} \in \partial V \right\}, \tag{2.11}$$

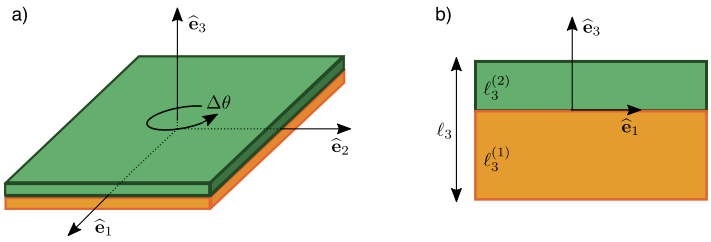

Fig. 2. (a) Geometry of a bilayer. The origin is placed at the interface of the two layers. (b) Cross-section of the bilayer in the $1-3$ plane. The volume fraction of each phase is $c=\ell_3^{(1)}/\ell_3$ and $1-c=\ell_3^{(2)}/\ell_3$.

with $\mathbf{e}_a$ denoting the applied electric field given by (2.2) (see Fig. 1b). It is worth noting here that contrary to the vector potential formulation presented in the previous section, the independent variable used in the potential energy in (2.10) is the electric field $\mathbf{e}$ (or equivalently the scalar potential φ). This implies that the application of $\mathbf{e}_a$ on the boundary of the LC corresponds to a Dirichlet BVP and thus the corresponding boundary term for the electric field appears in the constraint set (2.11).

The potential energy (2.10) is then extremized with respect to $\mathbf{n}$ and φ to give the equilibrium, the Gauss equations and the corresponding jump conditions at internal interfaces, which read (Pampolini and Triantafyllidis, 2018)

$$(\mathcal{P}_e)_{,\mathbf{n}}\delta\mathbf{n}=0 \;\Rightarrow\; \boldsymbol{\nabla}\cdot\frac{\partial w_e}{\partial\boldsymbol{\nabla}\mathbf{n}}-\frac{\partial w_e}{\partial\mathbf{n}}=\mathbf{0},\quad \forall\mathbf{x}\in V,\qquad \left[\!\!\left[\frac{\partial w_e}{\partial\boldsymbol{\nabla}\mathbf{n}}\right]\!\!\right]\mathbf{N}_i=\mathbf{0},\quad [\![\mathbf{n}]\!]=0,\quad \forall\mathbf{x}\in\partial V_r, \tag{2.12}$$

$$(\mathcal{P}_e)_{,\varphi}\delta\varphi=0 \;\Rightarrow\; \boldsymbol{\nabla}\cdot\mathbf{d}=\mathbf{0},\quad \mathbf{d}=-\frac{\partial w_e}{\partial\mathbf{e}},\quad \forall\mathbf{x}\in V,\qquad \mathbf{N}_i\cdot[\![\mathbf{d}]\!]=0,\quad \forall\mathbf{x}\in\partial V_r, \tag{2.13}$$

as well as the Dirichlet boundary conditions

$$\mathbf{n}=\mathbf{n}_{\partial V},\qquad \varphi(\mathbf{x})=\mathbf{e}_a\cdot\mathbf{x},\quad \forall\mathbf{x}\in\partial V. \tag{2.14}$$

Note further that to the field equations (2.12), one needs to consider also the unit-vector constraint described in (2.4).

It is important to mention at this point that the potential energies (2.3) and (2.10) are appropriate for the BVP shown in Fig. 1b, which corresponds to an applied electric field, $\mathbf{e}_a$ via electrodes directly attached to the external surfaces of the LC device. If instead one is interested to work with magnetically activated LCs, where the magnetic field is applied far from the device or not directly on its upper/lower surfaces, the more general expression (2.1) should be used and the surrounding air should be modeled as depicted in Fig. 1a. The reader is referred to the recent work of Danas (2017), Lefèvre et al. (2017) and Keip and Rambausek (2017) for a more detailed discussion of this point. Finally, both potential energies (2.3) and (2.10) can be augmented to include the polarization as an additional degree of freedom thus recovering the variational formulations of Sfyris et al. (2016) and Pampolini and Triantafyllidis (2018).

3. Material selection, ground state and principal solution

In the present work, we restrict attention to a two-phase ($L=2$) LC bilayer geometry, shown in Fig. 2. Henceforth, we use the superscript r to distinguish each phase ($r=1,2$). The two LC materials are separated by an interface defined by the normal $\mathbf{N}=\widehat{\mathbf{e}}_3$, while each layer has thickness along the x_3-direction, $\ell_3^{(r)}$ with $r=1,2$. For convenience, we set the origin $x_3=0$ at the interface of the two materials, such that $x_3\in[-\ell_3^{(1)},\ell_3^{(2)}]$ and $\ell_3=\ell_3^{(1)}+\ell_3^{(2)}$. The volume fraction of phase 1 is then denoted as $c=\ell_3^{(1)}/\ell_3$ whereas that of phase 2 is $1-c=\ell_3^{(2)}/\ell_3$.

3.1. Constitutive laws

The proposed LC bilayer geometry constitutes a theoretical model problem, that allows us to explore the richness of responses that one can obtain with such LC assemblies. Furthermore, following the existing literature, we assume that the free energy density of each phase, $w_e^{(r)}$ (or $w_d^{(r)}$, $r=1,2$) can be split in two parts; the mechanical free energy density, $\psi_m^{(r)}$, which is a function of the orientation of the director vector $\mathbf{n}(\mathbf{x})$ and its gradient $\boldsymbol{\nabla}\mathbf{n}(\mathbf{x})$, and the electrical part, $\psi_e^{(r)}$ (or $\psi_d^{(r)}$), which depends on $\mathbf{n}(\mathbf{x})$ and the electric field $\mathbf{e}(\mathbf{x})$ (or electric displacement $\mathbf{d}(\mathbf{x})$) but not on $\boldsymbol{\nabla}\mathbf{n}$. Hence, one can write

$$w_e^{(r)}(\mathbf{n}(\mathbf{x}),\boldsymbol{\nabla}\mathbf{n}(\mathbf{x}),\mathbf{e}(\mathbf{x}))=\psi_m^{(r)}(\mathbf{n}(\mathbf{x}),\boldsymbol{\nabla}\mathbf{n}(\mathbf{x}))+\psi_e^{(r)}(\mathbf{n}(\mathbf{x}),\mathbf{e}(\mathbf{x}))-\frac{\varepsilon_0}{2}\mathbf{e}(\mathbf{x})\cdot\mathbf{e}(\mathbf{x}),\quad r=1,2, \tag{3.1}$$

where again the dependence on $\mathbf{x}$ will be dropped for simplicity. The electrical energy is written in such a manner that if a given phase r has zero electric susceptibility then $\psi_e^{(r)}=0$, while still the last term in (3.1) is present to describe the background electric field energy in vacuum.

In view of this, we consider that the purely mechanical part of each phase is described by the well-known "Frank-Oseen" (FO) energy, which is given by

$$\psi_m^{(r)}(\mathbf{n},\nabla\mathbf{n})=\frac{1}{2}k_1^{(r)}\left(\nabla\cdot\mathbf{n}\right)^2+\frac{1}{2}k_2^{(r)}\left(\mathbf{n}\cdot\left(\nabla\times\mathbf{n}\right)+\tau^{(r)}\right)^2+\frac{1}{2}k_3^{(r)}\left\|\mathbf{n}\times\nabla\times\mathbf{n}\right\|^2. \tag{3.2}$$

Here, $k_1^{(r)}$, $k_2^{(r)}$ and $k_3^{(r)}$ are positive experimentally-obtained constants that serve to describe the *splay, twist* and *bending* deformation of the LC, respectively. In turn, $\tau^{(r)}$ is constant per phase and denotes the initial twist of the director field in the ground state. It appears in definition (3.2) as a prestress-type term, such that the overall energy is null in the ground state. Finally, in the last term of (3.2), $\|.\|$ denotes the Euclidean norm. The cases of a nematic and TN LC correspond to $\tau^{(r)}=0$ and $\tau^{(r)}\neq 0$, respectively. The evaluation of each $\tau^{(r)}$ for each phase given an overall twist of the bilayer is discussed in the following section.

Following Stewart (2004), we consider that the electromechanical energy of each phase is anisotropic and is given by a simple quadratic form in terms of $\mathbf{e}$, which reads

$$\psi_e^{(r)}(\mathbf{n},\mathbf{e})=-\frac{\varepsilon_0}{2}\mathbf{e}\cdot\boldsymbol{\chi}_e^{(r)}(\mathbf{n})\cdot\mathbf{e},\quad \boldsymbol{\chi}_e^{(r)}(\mathbf{n})=\chi_{\parallel}^{(r)}\mathbf{nn}+\chi_{\perp}^{(r)}(\mathbf{I}-\mathbf{nn}), \tag{3.3}$$

where $\boldsymbol{\chi}_e^{(r)}$ is the second-order tensor of the electric susceptibility given in terms of the parallel, $\chi_{\parallel}^{(r)}$, and perpendicular, $\chi_{\perp}^{(r)}$, to $\mathbf{n}$ components.

For completeness, we also recall the standard definition for the polarization vector

$$\mathbf{d}=\varepsilon_0\mathbf{e}+\mathbf{p}. \tag{3.4}$$

Using $(2.13)_2$ and (3.4), one obtains

$$\mathbf{d}=-\frac{\partial w_e^{(r)}}{\partial\mathbf{e}}=\varepsilon_0\left(\mathbf{I}+\boldsymbol{\chi}_e^{(r)}\right)\cdot\mathbf{e},\qquad \mathbf{p}=-\frac{\partial\psi_e^{(r)}}{\partial\mathbf{e}}=\varepsilon_0\boldsymbol{\chi}_e^{(r)}\cdot\mathbf{e}. \tag{3.5}$$

Next, using the partial Legendre-Fenchel transform in $(2.9)_2$, we readily find

$$w_d^{(r)}(\mathbf{n},\nabla\mathbf{n},\mathbf{d})=\psi_m^{(r)}(\mathbf{n},\nabla\mathbf{n})+\psi_d^{(r)}(\mathbf{n},\mathbf{d})+\frac{1}{2\,\varepsilon_0}\mathbf{d}\cdot\mathbf{d}, \tag{3.6}$$

with

$$\psi_d^{(r)}(\mathbf{n},\mathbf{d})=-\frac{1}{2\varepsilon_0}\mathbf{d}\cdot\boldsymbol{\chi}_d^{(r)}(\mathbf{n})\cdot\mathbf{d},\quad \boldsymbol{\chi}_d^{(r)}(\mathbf{n})=\boldsymbol{\chi}_e^{(r)}\cdot\left(\mathbf{I}+\boldsymbol{\chi}_e^{(r)}\right)^{-1}=\frac{\chi_{\perp}^{(r)}}{\chi_{\perp}^{(r)}+1}\mathbf{nn}+\frac{\chi_{\parallel}^{(r)}}{\chi_{\parallel}^{(r)}+1}(\mathbf{I}-\mathbf{nn}). \tag{3.7}$$

Combining relations $(2.7)_2$ and (3.4), one has

$$\mathbf{e}=\frac{\partial w_d^{(r)}}{\partial\mathbf{d}}=\varepsilon_0^{-1}\left(\mathbf{I}-\boldsymbol{\chi}_d^{(r)}\right)\cdot\mathbf{d},\qquad \mathbf{p}=-\varepsilon_0\frac{\partial\psi_d^{(r)}}{\partial\mathbf{d}}=\boldsymbol{\chi}_d^{(r)}\cdot\mathbf{d}. \tag{3.8}$$

The above-discussed constitutive relations can be easily modified to include saturation but this is beyond the scope of the present study.

3.2. Ground state for the director field for an overall twist $\Delta\theta$

In this section, we discuss the process of obtaining the ground state of the director field $\mathbf{n}(\mathbf{x})$ given an overall twist $\Delta\theta\neq 0$ between the upper and lower plates of the LC bilayer. This is a process that takes place during the fabrication of the LC device, before any electric field is applied to the system. Specifically, in the present study, the two nematic layers (i.e., with no initial twist) are initially placed together, separated by an interface, which is assumed to be perfect, i.e., both the director field and its gradient are continuous across that interface. Subsequently, an overall twist angle $\Delta\theta$ is applied about the x_3-axis at the upper and lower plates of the LC bilayer. In agreement with the literature for single LC layers (Stewart, 2004), the twist operation can be described by the minimization of the reduced potential energy

$$\mathcal{P}_\tau(\mathbf{n},\nabla\mathbf{n})=\inf_{\mathbf{n}\in\mathcal{S}}\sum_{r=1,2}\int_{V_r}w_\tau^{(r)}(\mathbf{n},\nabla\mathbf{n})\mathrm{d}V,\qquad w_\tau^{(r)}(\mathbf{n},\nabla\mathbf{n})=\frac{1}{2}k_2^{(r)}\left(\mathbf{n}\cdot\left(\nabla\times\mathbf{n}\right)\right)^2, \tag{3.9}$$

with $\mathcal{S}$ given by (2.4). The reduced energy w_τ derives from the FO energy (3.2) by keeping only the twist term $k_2^{(r)}$ and by setting $\tau^{(r)}=0$. Following the twist operation, the LC bilayer is allowed to come to a complete rest leading to its twisted ground state. In this ground state, the bilayer is described by the complete FO energy (3.2) with non-zero $\tau^{(r)}$ (Stewart, 2004). The above described process is consistent with the corresponding twisted ground states of LC single layers

reported in numerous studies in the literature, and is used in the following to evaluate the twist of the directors in each phase of for the LC bilayer.

Specifically, we consider the strong anchoring conditions defined in (2.4). For simplicity, we assign $\mathbf{n}(x_1, x_2, -\ell_3^{(1)}) = \widehat{\mathbf{e}}_1$ at the lower face of the LC bilayer. In turn, we apply a twist about the x_3-axis at the top face, such that $\mathbf{n}(x_1, x_2, \ell_3^{(2)}) = \cos\Delta\theta\,\widehat{\mathbf{e}}_1 + \sin\Delta\theta\,\widehat{\mathbf{e}}_2$, where $\Delta\theta$ is a constant denoting the overall twist angle, as shown in Fig. 2. In order to obtain the ground state for the director field $\mathbf{n}(\mathbf{x})$, we need to minimize (3.9) as well as satisfy the interface conditions in $(2.6)_{2,3}$ (with $\mathbf{N} = \widehat{\mathbf{e}}_3$) and the anchoring conditions in (2.4). Starting by the latter, we propose a trial director field that is independent of x_1 and x_2, such that

$$\mathbf{n}^{(r)} = \cos\left[\tau^{(r)}x_3 + t^{(r)}\right]\widehat{\mathbf{e}}_1 + \sin\left[\tau^{(r)}x_3 + t^{(r)}\right]\widehat{\mathbf{e}}_2, \quad r = 1, 2, \tag{3.10}$$

where $\tau^{(r)}$ is the twist of the director field in each phase and $t^{(r)}$ are constants. It is a matter of simple algebra to show that the director field (3.10) satisfies identically the equilibrium conditions (2.12) (or (2.6)) and thus extremizes (3.9). In turn, the four unknown constants in (3.10) shall be obtained by using the two anchoring conditions (described above) as well as the two interface conditions defined in (2.6).

In view of this, application of the director field (3.10) to the interface condition $(2.6)_2$ and use of the reduced energy(3.9) leads to

$$\left[\frac{\partial w_\tau^{(1)}}{\partial\nabla\mathbf{n}} - \frac{\partial w_\tau^{(2)}}{\partial\nabla\mathbf{n}}\right]\cdot\widehat{\mathbf{e}}_3 = \mathbf{0} \;\Rightarrow\; k_2^{(1)}\tau^{(1)} - k_2^{(2)}\tau^{(2)} = 0. \tag{3.11}$$

Using next the anchoring conditions at $x_3 = -\ell_3^{(1)}$ and $x_3 = \ell_3^{(2)}$, one gets

$$-\tau^{(1)}\ell_3^{(1)} + t^{(1)} = 0, \qquad \tau^{(2)}\ell_3^{(2)} + t^{(2)} = \Delta\theta. \tag{3.12}$$

Applying the continuity of the director field $\mathbf{n}$ at the interface $x_3 = 0$ (see equation $(2.6)_3$), we have

$$[\![\mathbf{n}]\!] = 0 \;\Rightarrow\; t^{(1)} = t^{(2)}, \tag{3.13}$$

which completes the set of equations necessary to evaluate $\tau^{(r)}$ and $t^{(r)}$. By solving the set of the four linear algebraic equations (3.11), (3.12) and (3.13), we finally obtain

$$\tau^{(1)} = \frac{k_2^{(2)}\,\Delta\theta}{k_2^{(2)}\,\ell_3^{(1)} + k_2^{(1)}\,\ell_3^{(2)}}, \quad \tau^{(2)} = \frac{k_2^{(1)}\,\Delta\theta}{k_2^{(2)}\,\ell_3^{(1)} + k_2^{(1)}\,\ell_3^{(2)}}, \quad t^{(1)} = \tau^{(1)}\ell_3^{(1)}, \quad t^{(2)} = \Delta\theta - \tau^{(2)}\ell_3^{(2)}. \tag{3.14}$$

Thus, the ground state solution for the director field becomes

$$\mathbf{n}_{gs}(\mathbf{x}) = \begin{cases} \cos\left[\tau^{(1)}\left(x_3 + \ell_3^{(1)}\right)\right]\widehat{\mathbf{e}}_1 + \sin\left[\tau^{(1)}\left(x_3 + \ell_3^{(1)}\right)\right]\widehat{\mathbf{e}}_2, & -\ell_3^{(1)} \le x_3 < 0, \\ \cos\left[\tau^{(2)}\left(x_3 - \ell_3^{(2)}\right) + \Delta\theta\right]\widehat{\mathbf{e}}_1 + \sin\left[\tau^{(2)}\left(x_3 - \ell_3^{(2)}\right) + \Delta\theta\right]\widehat{\mathbf{e}}_2, & 0 \le x_3 < \ell_3^{(2)}. \end{cases} \tag{3.15}$$

It is straightforward to show that the vector field (3.15) satisfies the equilibrium, jump and boundary conditions in (2.6) (or (2.12)) in the absence of an electric field. The ground state solution for the director vector is an initial piecewise uniform helix about the x_3-axis, where all directors lie in planes parallel to the end plates ($n_3 = 0$). It is also straightforward to show that the above ground state is an overall minimum leading to an overall zero FO energy defined in (3.6) for vanishing electric fields. It is important to mention at this point that we can recover easily the corresponding ground states reported for single layers (Sfyris et al., 2016; Stewart, 2004) by simply setting $k_2^{(1)} = k_2^{(2)}$ (and for simplicity $\ell_3^{(1)} = 0$, $\ell_3^{(2)} = \ell_3$) in (3.14), i.e. $\tau^{(1)} = \tau^{(2)} = \Delta\theta/\ell_3$ and $t^{(1)} = t^{(2)} = 0$.

Two representative examples of the ground state solution (3.15) are shown in Fig. 3. Layer 1 corresponds to an 7E material with $k_2^{(1)} = 5.82$pN and layer 2 to a 5CB material with $k_2^{(2)} = 3.9$pN. For illustration purposes $\ell_1 = \ell_3 = 1\mu$m, while the angle θ denotes the $1-2$ in-plane rotation of the directors. In Fig. 3a, we consider a bilayer with equal volume fraction for each phase, i.e., $c = 0.5$, and overall twist $\Delta\theta = \pi/2$, while in Fig. 3b, $c = 0.7$ and $\Delta\theta = 3\pi/2$. The interface separating the two layers is depicted with a dashed (green) line and corresponds always to the origin of the x_3 axis.

3.3. Principal solution for the director and the electric fields

In this section, we find the principal solution for $\mathbf{n}_0(\mathbf{x})$ and $\mathbf{d}_0$ (and $\mathbf{e}_0$) when an electric field $\mathbf{e}_a$ (*c.f.* (2.2)) is applied across the thickness of the LC bilayer. In this case, and following previous work for a single layer (Sfyris et al., 2016), one can easily show that the principal solution (i.e., before bifurcation) for the director field is exactly that of the ground state, i.e.,

$$\mathbf{n}_0(\mathbf{x}) = \mathbf{n}_{gs}(\mathbf{x}), \tag{3.16}$$

with $\mathbf{n}_{gs}$ given by (3.15). In other words, the directors retain their ground state up to bifurcation.

In turn, as a direct consequence of the jump conditions, defined in (2.13), the electric displacement is constant and equal in both layers, i.e., $\mathbf{d}_0(\mathbf{x}) = d_0\widehat{\mathbf{e}}_3$. By using (2.5) and (2.7), the minimum of the potential energy (2.3) admits a principal solution for the vector potential and the electric displacement given by

$$\boldsymbol{\alpha}_0(\mathbf{x}) = \frac{d_0}{2}(x_1\widehat{\mathbf{e}}_2 - x_2\widehat{\mathbf{e}}_1) \;\Rightarrow\; \mathbf{d}_0(\mathbf{x}) = \nabla\times\boldsymbol{\alpha}_0(\mathbf{x}) = \mathbf{d}_0^{(1)} = \mathbf{d}_0^{(2)} = d_0\widehat{\mathbf{e}}_3, \quad \forall\mathbf{x}\in V, \tag{3.17}$$

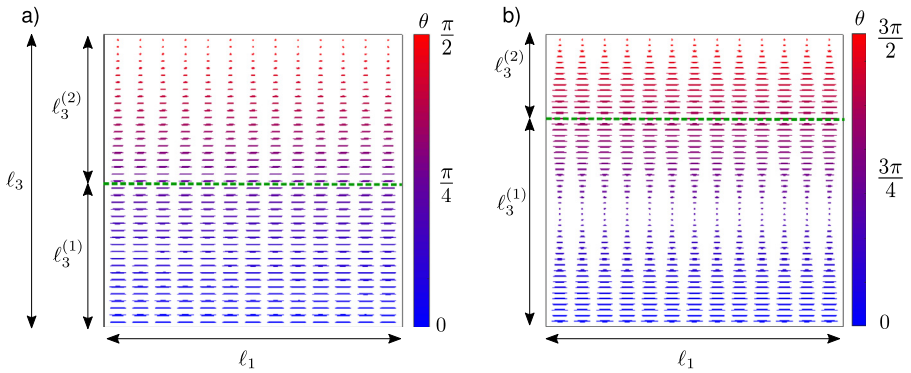

Fig. 3. Examples of ground state solutions for the director vector $\mathbf{n}_{gs}$ for (a) $c = 0.5$ and $\Delta\theta = \pi/2$ and (b) $c = 0.7$ and $\Delta\theta = 3\pi/2$. Layer 1 corresponds to an 7E material with $k_2^{(1)} = 5.82$pN and layer 2 to a 5CB material with $k_2^{(2)} = 3.9$pN. For illustration purposes $\ell_1 = \ell_3 = 1\,\mu$m. The angle θ denotes the $1-2$ in-plane rotation of the directors. The interface separating the two layers is denoted with a dashed (green) line. (For interpretation of the references to colour in this figure legend, the reader is referred to the web version of this article.)

which by use of (2.2) becomes

$$d_0\widehat{\mathbf{e}}_3 = \varepsilon_0\mathbf{e}_a = \varepsilon_0\frac{\Delta\varphi_a}{\ell_3}\widehat{\mathbf{e}}_3. \tag{3.18}$$

On the other hand, the electric field, $\mathbf{e}(\mathbf{x})$, and the polarization, $\mathbf{p}(\mathbf{x})$, exhibit jumps across the bilayer interface but remain constant inside each layer. Using relations (3.4), (2.11), (2.12) and the constitutive relations (3.5) and (3.8), we find the following principal solution for the electric potential and corresponding electric fields in the bilayer in terms of the applied electric field $\mathbf{e}_a$,

$$\varphi_0(\mathbf{x}) = \begin{cases} \mathbf{e}_0^{(1)}\cdot\mathbf{x}, & -\ell_3^{(1)} \le x_3 < 0, \\ \mathbf{e}_0^{(2)}\cdot\mathbf{x}, & 0 \le x_3 < \ell_3^{(2)}, \end{cases} \qquad \mathbf{e}_0^{(r)} = \frac{1}{\chi_\perp^{(r)}+1}\mathbf{e}_a, \qquad \mathbf{p}_0^{(r)} = \frac{\varepsilon_0\chi_\perp^{(r)}}{\chi_\perp^{(r)}+1}\mathbf{e}_a, \tag{3.19}$$

with $\mathbf{e}_a$ given by (2.2). Notice that the principal solutions for the electric displacement $\mathbf{d}$, the electric field $\mathbf{e}$ and the polarization vector $\mathbf{p}$ depend only on x_3.

4. The numerical bifurcation problem: critical electric fields and eigenmodes

4.1. Bifurcation functional

Of interest here is the stability of the principal solution presented in the previous section and more precisely the onset of first bifurcation at the lowest electric field $\mathbf{e}_a$. As shown in (3.18), the actual applied load is the potential difference $\Delta\varphi_a$, but for simplicity in the subsequent presentation, d_0 will be referred to henceforth as the applied *load* (*c.f.* (3.18)).

The latter is obtained by minimizing the potential energy $\mathcal{P}_d \equiv \mathcal{P}$ (for simplicity of notation henceforth) in (2.3) with respect to the independent variables, denoted compactly by $\mathbf{g} \equiv \{\mathbf{n}, \boldsymbol{\alpha}\}$. This solution depends on the applied electric displacement d_0 (or equivalently on the potential difference $\Delta\varphi_a$). At relatively small values of the applied load d_0, the principal solution $\mathbf{g}_0(d_0)$ (*c.f.* (3.15) and (3.17)) is stable, i.e. it is a local minimizer of the potential energy satisfying $(\mathcal{P}_{,\mathbf{gg}}(\mathbf{g}_0(d_0), d_0)\Delta\mathbf{g})\delta\mathbf{g} > 0$, for arbitrary perturbations $\delta\mathbf{g} \neq \mathbf{0}$. As the applied load increases, it reaches a critical value d_0^c, where the principal solution at hand $\mathbf{g}_0(d_0^c)$ is no longer a local minimizer, whereby non-uniform electric fields as well as out-of-plane components of the director $\mathbf{n}$ (i.e. $n_3 \neq 0$) emerge in the LC bilayer. At that point, also known as the *Freedericksz transition*, the second variation of the energy vanishes along a particular direction $\Delta\mathbf{g}$, which satisfies the condition:

$$\delta\Delta\mathcal{P} \equiv (\mathcal{P}_{,\mathbf{gg}}(\mathbf{g}_0(d_0^c), d_0^c)\Delta\mathbf{g})\delta\mathbf{g} = 0. \tag{4.1}$$

Here, $\Delta\mathbf{g}$ is the bifurcation eigenmode, and $\delta\mathbf{g}$ denotes the arbitrary test functions corresponding to the independent variables of the problem, $\mathbf{g}$. In the following, we calculate the bilinear operator $\delta\Delta\mathcal{P}$ using the energy functions defined in Section 3.

Before, calculating the second variation in (4.1), it is important to take into account in the potential energy (2.3) the constraint of $\mathbf{n}\cdot\mathbf{n} = 1$ introduced in (2.4) as well as the Coulomb gauge $\nabla\cdot\boldsymbol{\alpha} = 0$ discussed in (2.5). In view of the numerical algorithm adopted in the present study, we choose to introduce these constraints by using a penalty method, which has the advantage of preserving the positive definiteness of the potential energy, while being easy to implement numerically. By

expanding the constitutive relations (3.6)–(3.8), the potential energy in (2.3) becomes

$$\mathcal{P}(\mathbf{n},\boldsymbol{\alpha}) = \frac{1}{2}\sum_{r=1,2}\int_{V_r}\Big[k_1^{(r)}\big(\boldsymbol{\nabla}\cdot\mathbf{n}\big)^2 + k_2^{(r)}\left(\mathbf{n}\cdot\big(\boldsymbol{\nabla}\times\mathbf{n}\big)+\tau^{(r)}\right)^2 + k_3^{(r)}\,\|\mathbf{n}\times\boldsymbol{\nabla}\times\mathbf{n}\|^2 + \frac{C_a^{(r)}}{\varepsilon_0}\|(\boldsymbol{\nabla}\times\boldsymbol{\alpha})\cdot\mathbf{n}\|^2 + \frac{C_\perp^{(r)}}{\varepsilon_0}\|\boldsymbol{\nabla}\times\boldsymbol{\alpha}\|^2 + \frac{k^{(r)}}{\ell_3^2\,\xi_n^{(r)}}(\mathbf{n}\cdot\mathbf{n}-1)^2 + \frac{1}{\varepsilon_0\,\xi_\alpha^{(r)}}(\boldsymbol{\nabla}\cdot\boldsymbol{\alpha})^2\Big]\mathrm{d}V + \int_{\partial V}\varepsilon_0^{-1}d_0(\widehat{\mathbf{e}}_3\times\boldsymbol{\alpha})\cdot\mathbf{N}\,\mathrm{d}S. \tag{4.2}$$

Here, we have introduced the notation $C_\perp^{(r)} \equiv (\chi_\perp^{(r)}+1)^{-1}$ and $C_a^{(r)} \equiv (\chi_\perp^{(r)}-\chi_\parallel^{(r)})\,(\chi_\perp^{(r)}+1)^{-1}\,(\chi_\parallel^{(r)}+1)^{-1}$, and $k^{(r)} = \sqrt{\sum_{j=1,3}(k_j^{(r)})^2}$. The two positive constants $\xi_n^{(r)} \ll 1$ and $\xi_\alpha^{(r)} \ll 1$ are penalty factors serving to enforce the relevant constraints and shall take sufficiently small values to be defined later. The addition of ℓ_3 and ε_0 in the last two term of (4.2) allows for the non-dimensionalization of these terms.

In the following, we consider the perturbations $\delta\mathbf{g} = (\delta\mathbf{n}, \delta\boldsymbol{\alpha})$ about the principal solutions $\mathbf{n}_0$ and $\boldsymbol{\alpha}_0$ defined in equations (3.15) and (3.17), respectively. Those perturbations, $\delta\mathbf{g}$, as well as the corresponding eigenmodes $\Delta\mathbf{g}$ satisfy the essential boundary conditions for $\mathbf{n}$, which belongs to the admissible set $\mathcal{S}$ (see Eq. (2.4)). This implies

$$\Delta\mathbf{n}(x_1,x_2,-\ell_3^{(1)}) = \delta\mathbf{n}(x_1,x_2,-\ell_3^{(1)}) = \Delta\mathbf{n}(x_1,x_2,\ell_3^{(2)}) = \delta\mathbf{n}(x_1,x_2,\ell_3^{(2)}) = 0. \tag{4.3}$$

Next, by noting that the director is a unit vector (i.e. $\mathbf{n}_0\cdot\mathbf{n}_0 = \mathbf{n}\cdot\mathbf{n} = 1$) and $\mathbf{n}_0$ and $\boldsymbol{\alpha}_0$ are the principal solutions described in equations (3.15) and (3.17), respectively, we write the identities

$$\mathbf{n}_0\cdot\Delta\mathbf{n} = \mathbf{n}_0\cdot\delta\mathbf{n} = 0, \quad \boldsymbol{\nabla}\cdot\mathbf{n}_0 = 0, \quad \boldsymbol{\nabla}\times\mathbf{n}_0 + \tau^{(r)}\mathbf{n}_0 = 0, \quad \mathbf{n}_0\times\boldsymbol{\nabla}\times\mathbf{n}_0 = \mathbf{0}, \quad (\boldsymbol{\nabla}\times\boldsymbol{\alpha}_0)\cdot\mathbf{n}_0 = 0. \tag{4.4}$$

Use of these identities, allows us to write the second variation of (4.1) evaluated at the principal path, in the explicit form

$$\Delta\delta\mathcal{P}(d_0)|_{\mathbf{n}_0,\boldsymbol{\alpha}_0} = \sum_{r=1,2}\int_{V_r}\Big[\mathcal{L}_{ij}^{nn,(r)}\Delta n_i\delta n_j + \mathcal{L}_{ijkl}^{\nabla n\nabla n,(r)}\Delta n_{i,j}\delta n_{k,l} + \mathcal{L}_{ijk}^{\nabla nn,(r)}(\Delta n_{i,j}\delta n_k + \Delta n_k\delta n_{i,j}) + \mathcal{L}_{ijk}^{\nabla\alpha n,(r)}(\Delta\alpha_{i,j}\delta n_k + \Delta n_k\delta\alpha_{i,j}) + \mathcal{L}_{ijkl}^{\nabla\alpha\nabla\alpha,(r)}\Delta\alpha_{i,j}\delta\alpha_{k,l}\Big]\mathrm{d}V, \tag{4.5}$$

where the subscripts *i, j, k, l* denote components with respect to the Cartesian coordinate system. The incremental moduli in (4.5) are given by

$$\begin{aligned}
\mathcal{L}_{ij}^{nn,(r)} &= k_3^{(r)}(\tau^{(r)})^2\delta_{ij} + \frac{k^{(r)}}{\ell_3\xi_n^{(r)}}(n_0^{(r)})_i\,(n_0^{(r)})_j + \frac{C_a^{(r)}}{\varepsilon_0}d_0^2\delta_{i3}\delta_{j3},\\
\mathcal{L}_{ijk}^{\nabla nn,(r)} &= -\tau^{(r)}k_3^{(r)}\varepsilon_{ijk},\\
\mathcal{L}_{ijkl}^{\nabla n\nabla n,(r)} &= k_1^{(r)}\delta_{ij}\delta_{kl} + (k_2^{(r)}-k_3^{(r)})\varepsilon_{ijp}\varepsilon_{klq}(n_0^{(r)})_p\,(n_0^{(r)})_q + k_3^{(r)}(\delta_{ik}\delta_{jl}-\delta_{il}\delta_{jk}),\\
\mathcal{L}_{ijk}^{\nabla\alpha n,(r)} &= -\frac{C_a^{(r)}}{\varepsilon_0}d_0(n_0^{(r)})_p\varepsilon_{pij}\delta_{k3},\\
\mathcal{L}_{ijkl}^{\nabla\alpha\nabla\alpha,(r)} &= \frac{C_\perp^{(r)}}{\varepsilon_0}(\delta_{ik}\delta_{jl}-\delta_{il}\delta_{jk}) + \frac{C_a^{(r)}}{\varepsilon_0}\varepsilon_{ijp}\varepsilon_{klq}(n_0^{(r)})_p\,(n_0^{(r)})_q + \frac{1}{\varepsilon_0\,\xi_\alpha^{(r)}}\delta_{ij}\delta_{kl},
\end{aligned} \tag{4.6}$$

with d_0 defined by (3.18). In this last relation, we have explicitly used the notation $\mathbf{n}_0{}^{(r)}$ to denote the principal solution for the director field within each layer $r = 1, 2$, given by (3.15), δ_{ij} denotes the Kronecker identity second order tensor and ε_{ijk} the permutation symbol.

4.2. Finite-Element (FE) discretization and calculations

The eigenvalue problem (4.1) together with the boundary conditions (4.3) is solved numerically by considering the Fourier transform of $\Delta\mathbf{g}$ in the x_1 and x_2 directions ($\mathbb{R}^2$) and a finite-element discretization along x_3. For the special case of no twist, $\Delta\theta = \tau^{(1)} = \tau^{(2)} = 0$, an analytical solution is presented in the following Section.

We consider then the eigenmodes $\Delta\mathbf{g}$ (and similarly the test functions $\delta\mathbf{g}$)

$$\Delta\mathbf{n}(x_1,x_2,x_3) = \Delta\mathcal{N}(x_3)\exp[\mathrm{i}(\omega_1x_1+\omega_2x_2)], \quad \Delta\boldsymbol{\alpha}(x_1,x_2,x_3) = \Delta\mathcal{A}(x_3)\exp[\mathrm{i}(\omega_1x_1+\omega_2x_2)], \tag{4.7}$$

and substitute them in (4.5). After some tedious but straightforward algebra, we find

$$\Delta\delta\mathcal{P}(d_0) = \int_{\mathbb{R}^2}\left[\int_{-\ell_3^{(1)}}^{0}\mathcal{I}^{(1)}(\omega_1,\omega_2,x_3;d_0)\mathrm{d}x_3 + \int_0^{\ell_3^{(2)}}\mathcal{I}^{(2)}(\omega_1,\omega_2,x_3;d_0)\mathrm{d}x_3\right]\mathrm{d}\omega_1\mathrm{d}\omega_2, \tag{4.8}$$

with

$$\begin{aligned}\mathcal{I}^{(r)} \equiv\ & \mathcal{L}^{nn,(r)}_{ik}\Delta\overline{\mathcal{N}}_i\,\delta\mathcal{N}_k + \mathcal{L}^{\nabla nn,(r)}_{i3k}(\Delta\overline{\mathcal{N}}_{i,3}\delta\mathcal{N}_k + \Delta\overline{\mathcal{N}}_k\delta\mathcal{N}_{i,3}) + \mathrm{i}\,\omega_\beta\mathcal{L}^{\nabla nn,(r)}_{i\beta k}(\Delta\overline{\mathcal{N}}_k\delta\mathcal{N}_i - \Delta\overline{\mathcal{N}}_i\delta\mathcal{N}_k)\\ &+ \mathcal{L}^{\nabla n\nabla n,(r)}_{i3k3}\Delta\overline{\mathcal{N}}_{i,3}\delta\mathcal{N}_{k,3} - \mathrm{i}\omega_\beta\mathcal{L}^{\nabla n\nabla n,(r)}_{i\beta k3}\Delta\overline{\mathcal{N}}_i\delta\mathcal{N}_{k,3} + \mathrm{i}\omega_\beta\mathcal{L}^{\nabla n\nabla n,(r)}_{i3k\beta}\Delta\overline{\mathcal{N}}_{i,3}\delta\mathcal{N}_k + \omega_\beta\omega_\gamma\mathcal{L}^{\nabla n\nabla n,(r)}_{i\beta k\gamma}\Delta\overline{\mathcal{N}}_i\delta\mathcal{N}_k\\ &+ \mathcal{L}^{\nabla\alpha n,(r)}_{i3k}(\Delta\overline{\mathcal{A}}_{i,3}\delta\mathcal{N}_k + \Delta\overline{\mathcal{N}}_k\delta\mathcal{A}_{i,3}) + \mathrm{i}\,\omega_\beta\mathcal{L}^{\nabla nn,(r)}_{i\beta k}(\Delta\overline{\mathcal{N}}_k\delta\mathcal{A}_i - \Delta\overline{\mathcal{A}}_i\delta\mathcal{N}_k)\\ &+ \mathcal{L}^{\nabla\alpha\nabla\alpha,(r)}_{i3k3}\Delta\overline{\mathcal{A}}_{i,3}\delta\mathcal{A}_{k,3} - \mathrm{i}\omega_\beta\mathcal{L}^{\nabla\alpha\nabla\alpha,(r)}_{i\beta k3}\Delta\overline{\mathcal{A}}_i\delta\mathcal{A}_{k,3} + \mathrm{i}\omega_\beta\mathcal{L}^{\nabla\alpha\nabla\alpha,(r)}_{i3k\beta}\Delta\overline{\mathcal{A}}_{i,3}\delta\mathcal{A}_k + \omega_\beta\omega_\gamma\mathcal{L}^{\nabla\alpha\nabla\alpha,(r)}_{i\beta k\gamma}\Delta\overline{\mathcal{A}}_i\delta\mathcal{A}_k. \end{aligned} \tag{4.9}$$

In these expressions, a bar ($\overline{f}$) denotes complex conjugation of the quantity (f). From the Dirichlet conditions in (4.3) and (4.7), we obtain

$$\Delta\boldsymbol{\mathcal{N}}(-\ell_3^{(1)}) = \Delta\boldsymbol{\mathcal{N}}(\ell_3^{(2)}) = \delta\boldsymbol{\mathcal{N}}(-\ell_3^{(1)}) = \delta\boldsymbol{\mathcal{N}}(\ell_3^{(2)}) = 0. \tag{4.10}$$

The Neumann boundary conditions (2.8) together with (4.7) lead to

$$\Delta\mathcal{A}_3(-\ell_3^{(1)}) = \Delta\mathcal{A}_3(\ell_3^{(2)}) = \delta\mathcal{A}_3(-\ell_3^{(1)}) = \delta\mathcal{A}_3(\ell_3^{(2)}) = 0. \tag{4.11}$$

For the special case of $\omega_1 = \omega_2 = 0$ (i.e. the x_1, x_2 independent eigenmode problem), we need to impose additional constraints on $\Delta\boldsymbol{\mathcal{A}}$ (and $\delta\boldsymbol{\mathcal{A}}$), which read $\Delta\mathcal{A}_1(0) = \Delta\mathcal{A}_2(0) = 0$ (and $\delta\mathcal{A}_1(0) = \delta\mathcal{A}_2(0) = 0$). This eliminates trivial modes of the stiffness matrix in this special case.

A finite-element discretization of $\Delta\boldsymbol{\mathcal{A}}$ and $\Delta\boldsymbol{\mathcal{N}}$ for all $x_3 \in [-\ell_3^{(1)}, \ell_3^{(2)}]$ is employed to check the loss of positive definiteness of $\Delta\delta\mathcal{P}$ in (4.8) $\forall\{\omega_1, \omega_2\} \in \mathbb{R}^2$. The thickness of the LC bilayer then is divided in N_e segments (i.e. finite elements). Each finite element comprises two end nodes, each of which carries six degrees of freedom, denoted by the vector $[\Delta\mathbf{G}^I]^T \equiv [\Delta\mathcal{N}_1^I, \Delta\mathcal{N}_2^I, \Delta\mathcal{N}_3^I, \Delta\mathcal{A}_1^I, \Delta\mathcal{A}_2^I, \Delta\mathcal{A}_3^I]^T$ with $I = 1, N_e + 1$. Using standard FE manipulations, the functional (4.8) can be written in the form

$$\Delta\delta\mathcal{P}(d_0) = [\Delta\mathbf{G}]^T \cdot \mathbf{K}(\omega_1, \omega_2, d_0) \cdot [\delta\mathbf{G}]^T \tag{4.12}$$

where $[\Delta\mathbf{G}] = \left[[\Delta\mathbf{G}^1], [\Delta\mathbf{G}^2, \ldots, [\Delta\mathbf{G}^{N_e+1}]\right]$ is the global vector of the nodal degrees of freedom with dimension $\dim[\Delta\mathbf{G}] = 6(N_e + 1)$ and $\mathbf{K}$ is the corresponding stiffness matrix with dimensions $\dim[\mathbf{K}] = 6(N_e + 1) \times 6(N_e + 1)$. The stiffness matrix, $\mathbf{K}$, which is also called the *stability matrix*, is Hermitian, i.e. $\mathbf{K}^T = \overline{\mathbf{K}}$ and thus has real eigenvalues. It is recalled that the boundary conditions (4.10) and (4.11) have to be applied to $\mathbf{K}$ (otherwise it is singular). The application of these boundary conditions is done using an elimination technique.

In the absence of an electric field ($d_0 = 0$), the stability matrix $\mathbf{K}(\omega_1, \omega_2, 0)$ is always positive definite. For a chosen set of values $(\omega_1, \omega_2) \in \mathbb{R}^2$ and at a given value of the electric field $d_0^\omega(\omega_1, \omega_2) > 0$, the lowest eigenvalue of $\mathbf{K}$, denoted as $\lambda^K_{\min}(\omega_1, \omega_2, d_0^\omega)$, vanishes. This indicates a loss of stability of the system for the given set of $(\omega_1, \omega_2) \in \mathbb{R}^2$. The critical value of the electric field d_0^c (and the corresponding wavenumbers ω_1^c and ω_2^c) is the minimum of d_0^ω over $(\omega_1, \omega_2) \in \mathbb{R}^2$, namely

$$\lambda^K_{min}(\omega_1, \omega_2, d_0^\omega) = 0, \qquad d_0^c(\omega_1^c, \omega_2^c) = \min_{(\omega_1,\omega_2)\in\mathbb{R}^2} d_0^\omega(\omega_1, \omega_2). \tag{4.13}$$

In our numerical calculations, we parameterize the wavenumbers as $\omega_1 \equiv R\cos\Theta$ and $\omega_2 \equiv R\sin\Theta$, with $R \in \mathbb{R}^+$ and $\Theta \in [0, 2\pi)$. Due to the symmetry of the stability matrix, $\mathbf{K}(\omega_1, \omega_2, d_0) = \overline{\mathbf{K}}(-\omega_1, -\omega_2, d_0)$, we only need to scan half of the Θ interval. Specifically, we analyze the interval $(R, \Theta) \in [0, 20] \times [0, \pi]$ with increments $\Delta R = 0.1$ and $\Delta\Theta = \pi/180$. For each pair of (ω_1, ω_2), we increase d_0 away from zero by using large increments $\Delta d_0 = 10$ C $\cdot\mu\mathrm{m}^{-2}$ until $\lambda^K_{\min} < 0$. Then a bisection method is used recurrently until we satisfy the convergence criterion, defined by

$$\left\|\lambda^K_{min}(\omega_1, \omega_2, d_0|_j) - \lambda^K_{min}(\omega_1, \omega_2, d_0|_{j+1})\right\| \le 10^{-3}\lambda^K_{min}(d_0|_0), \tag{4.14}$$

where the subscript j indicates the iteration number. The scanning process is carried out for overall twists $\Delta\theta \in [0, 2\pi]$ with increments $\Delta\theta = 5\pi/180$ and for a large number of volume fractions c of the layers.

In the calculations reported here, we use the same dimensionless penalty parameters $\xi_n^{(r)} = \xi_\alpha^{(r)} = 10^{-6}$ for each phase $r = 1, 2$ in order to impose the unit length of the director vector $\mathbf{n}$ and the Coulomb gauge condition, as discussed in the potential energy definition (4.8). Such low values, however, lead to locking and hence an overly stiff system. We avoid locking, by a simple reduced integration scheme with one Gauss point per element for the integration of the Coulomb gauge and the unit length director constraints in the x_3 integrals appearing in (4.8). For the remaining terms in that integral, the integration is carried out using two Gauss points per element. All final calculations reported in this study use a total mesh size of $N_e = 60$ equal length elements which are partitioned proportionally to the volume fraction of each layer. In addition to the mesh size, the above referenced values of the penalty parameters as well as the adopted integration scheme are selected by requiring that the difference between the numerically calculated d_0^c, ω_1^c and ω_2^c and the analytical ones (available only for zero twist, i.e., $\Delta\theta = 0$), presented in the following section, is less than 0.1%.

5. An analytical solution for zero twist

In this section, we develop an analytical solution for the BVP depicted in Fig. 1b, comprising the LC bilayer of Fig. 2. This solution is obtained only for $\Delta\theta = 0$, while for any other twist angle the problem can only be analyzed numerically, as

discussed in the previous section. For simplicity in the subsequent algebraic manipulations, we rely on the scalar potential variational principle with respect to the variable $\mathbf{g}=\{\mathbf{n},\varphi\}$ defined in (2.10). By substituting the constitutive relations (3.1), (3.3) and (3.5) in (2.10), one obtains

$$\mathcal{P}_e(\mathbf{n},\varphi)=\frac{1}{2}\sum_{r=1,2}\int_{V_r}\Big[k_1^{(r)}\big(\boldsymbol{\nabla}\cdot\mathbf{n}\big)^2+k_2^{(r)}\big(\mathbf{n}\cdot\big(\boldsymbol{\nabla}\times\mathbf{n}\big)\big)^2+k_3^{(r)}\,\|\mathbf{n}\times\boldsymbol{\nabla}\times\mathbf{n}\|^2+ \\ -\frac{\varepsilon_0}{C_\perp^{(r)}}\boldsymbol{\nabla}\varphi\cdot\boldsymbol{\nabla}\varphi-\frac{\varepsilon_0}{C_b^{(r)}}(\boldsymbol{\nabla}\varphi\cdot\mathbf{n})^2\Big]\mathrm{d}V. \tag{5.1}$$

where $C_b^{(r)}\equiv(\chi_\parallel^{(r)}-\chi_\perp^{(r)})^{-1}$. The constraint of $\mathbf{n}$ being a unit vector is applied explicitly in the equations that follow and thus no penalty constraint need to be introduced in this case.

By referring to (3.15), we readily obtain the principal solution for the director field $\mathbf{n}_0(\mathbf{x})$ in the case of overall zero twist, i.e., $\Delta\theta=0$, which reads $\mathbf{n}_0(\mathbf{x})=\widehat{\mathbf{e}}_1$. The principal solutions φ_0 for $\mathbf{e}_0^{(r)}$ are given directly by equations (3.19) and are piecewise constant within each layer.

We consider next the perturbations $\delta\mathbf{g}=\{\delta\mathbf{n},\delta\varphi\}$ about the principal solutions $\mathbf{n}_0$ and φ_0. Note that $\delta\mathbf{n}$ and $\Delta\mathbf{n}$ should be admissible and thus must belong to the set $\mathcal{S}$ defined in (2.4). This implies that they must satisfy the anchoring conditions (4.3) at $x_3=-\ell_3^{(1)}$ and $x_3=\ell_3^{(2)}$. Similarly, $\delta\varphi$ and $\Delta\varphi$ belong to $\mathcal{E}$ (see (2.11)) and hence, they must satisfy the Dirichlet boundary conditions

$$\Delta\varphi(x_1,x_2,-\ell_3^{(1)})=\delta\varphi(x_1,x_2,-\ell_3^{(1)})=\Delta\varphi(x_1,x_2,\ell_3^{(2)})=\delta\varphi(x_1,x_2,\ell_3^{(2)})=0. \tag{5.2}$$

The bifurcation condition (4.1) holds also for the new set of independent variable $\mathbf{g}\equiv\{\mathbf{n},\varphi\}$. Again, by use of the identities (4.4), one may obtain the second variation of (5.1) in the explicit form

$$\delta\Delta\mathcal{P}_e(d_0)|_{\mathbf{n}_0,\varphi_0}=\sum_{r=1,2}\int_{V_r}\Big[\mathcal{L}_{ijkl}^{\nabla n\nabla n,(r)}\Delta n_{i,j}\delta n_{k,l}+\mathcal{L}_{ij}^{nn,(r)}\Delta n_i\delta n_j \\ +\mathcal{L}_{ij}^{n\nabla\varphi,(r)}(\Delta\varphi_{,i}\delta n_j+\Delta n_i\delta\varphi_{,j})+\mathcal{L}_{ij}^{\nabla\varphi\nabla\varphi,(r)}\Delta\varphi_{,i}\delta\varphi_{,j}\Big]\mathrm{d}V, \tag{5.3}$$

where the subscripts i, j, k, l represent components in the Cartesian coordinate system. The incremental modulus $\mathcal{L}_{ijkl}^{\nabla n\nabla n,(r)}$ of the above is the same as in $(4.6)_3$. The remaining incremental moduli in (5.3) are given by

$$\mathcal{L}_{ij}^{nn,(r)}=-\frac{\varepsilon_0}{C_b^{(r)}}(\varphi_0^{(r)})_{,i}(\varphi_0^{(r)})_{,j}, \\ \mathcal{L}_{ij}^{n\nabla\varphi,(r)}=-\frac{\varepsilon_0}{C_b^{(r)}}\big[(n_0^{(r)})_i(\varphi_0^{(r)})_{,j}+(\varphi_0^{(r)})_{,i}(n_0^{(r)})_j+(n_0^{(r)})_k(\varphi_0^{(r)})_{,k}\delta_{ij},\big] \\ \mathcal{L}_{ij}^{\nabla\varphi\nabla\varphi,(r)}=-\varepsilon_0\Big[\frac{1}{C_\perp^{(r)}}\delta_{ij}+\frac{1}{C_b^{(r)}}(n_0^{(r)})_i(n_0^{(r)})_j\Big]. \tag{5.4}$$

Again here, we have explicitly used the notation $\mathbf{n}_0{}^{(r)}$ to denote the principal solution for the director field within each layer $r=1,2$, given by (3.15). As a consequence of the arbitrariness of δn and $\delta\varphi$ in (5.3), we obtain the Euler–Lagrange equations for $\Delta\mathbf{n}$ and $\Delta\varphi$, which read

$$-\mathcal{L}_{ijkl}^{\nabla n\nabla n,(r)}\Delta n_{k,lj}+\mathcal{L}_{ij}^{nn,(r)}\Delta n_j+\mathcal{L}_{ij}^{n\nabla\varphi,(r)}\Delta\varphi_{,j}=0,\qquad \mathcal{L}_{ij}^{\nabla\varphi\nabla\varphi,(r)}\Delta\varphi_{,ij}+\mathcal{L}_{ij}^{n\nabla\varphi,(r)}\Delta n_{i,j}=0, \tag{5.5}$$

along with the interface conditions at $x_3=0$

$$[\![\Delta n_i]\!]=0,\qquad \Big[\!\Big[\mathcal{L}_{i3kl}^{\nabla n\nabla n,(r)}\Delta n_{k,l}\Big]\!\Big]=0,\quad [\![\Delta\varphi]\!]=0,\qquad \Big[\!\Big[\mathcal{L}_{3j}^{n\nabla\varphi,(r)}\Delta n_j+\mathcal{L}_{3j}^{\nabla\varphi\nabla\varphi,(r)}\Delta\varphi_{,j}\Big]\!\Big]=0. \tag{5.6}$$

The corresponding Dirichlet boundary conditions for $\Delta\mathbf{n}$ and $\Delta\varphi$ at the top and bottom faces of the LC bilayer defined in (4.3) and (5.2), respectively, must be added.

Next, using the constraint $\mathbf{n}\cdot\mathbf{n}=\mathbf{n}_0\cdot\mathbf{n}_0=1$, one can write $\Delta n_1(\mathbf{x})$ in terms of the other two components, i.e., $\Delta n_2(\mathbf{x})$ and $\Delta n_3(\mathbf{x})$ (Sfyris et al., 2016). The governing equations (5.5) admit a general solution

$$[\Delta n_2(\mathbf{x}),\Delta n_3(\mathbf{x}),\Delta\varphi(\mathbf{x})]=[\Delta\mathcal{N}_2^{(r)}(x_3),\mathrm{i}\Delta\mathcal{N}_3^{(r)}(x_3),\Delta\Phi^{(r)}(x_3)]\exp(\mathrm{i}\omega_1x_1+\mathrm{i}\omega_2x_2), \tag{5.7}$$

with

$$\begin{bmatrix} \Delta\mathcal{N}_2^{(r)}(x_3) & \Delta\mathcal{N}_3^{(r)}(x_3) & \Delta\Phi^{(r)}(x_3) \end{bmatrix} = \sum_{I=1,3} \begin{bmatrix} \xi_I^{s,(r)} & \xi_I^{c,(r)} \end{bmatrix}$$
$$\begin{bmatrix} \sinh(\rho_I^{(r)}x_3) & \cosh(\rho_I^{(r)}x_3) & \cosh(\rho_I^{(r)}x_3) \\ \cosh(\rho_I^{(r)}x_3) & \sinh(\rho_I^{(r)}x_3) & \sinh(\rho_I^{(r)}x_3) \end{bmatrix} \begin{bmatrix} \Delta\widehat{\mathcal{N}}_2^{I,(r)} & 0 & 0 \\ 0 & \Delta\widehat{\mathcal{N}}_3^{I,(r)} & 0 \\ 0 & 0 & 1 \end{bmatrix}. \tag{5.8}$$

In this last expression, $\xi_I^{c,(r)}$ and $\xi_I^{s,(r)}$ are the eigenmode amplitudes to be subsequently determined in this section from the boundary and interface conditions (4.3), (5.2) and (5.6).

In turn, $\rho_I^{(r)}$ and $\Delta\widehat{\mathcal{N}}^{I,(r)}$ are evaluated by substituting (5.7) and (5.8) in the governing equations (5.5). This leads to an eigenvalue problem

$$\mathbf{Q}^{(r)}(\omega_1, \omega_2, d_0, \rho_I^{(r)})\Delta\widehat{\mathcal{N}}^{I,(r)} = 0. \tag{5.9}$$

Here, $\mathbf{Q}^{(r)}$ is a 3×3 matrix, whose individual elements are derived in the electronic SM. A non-trivial solution for the system (5.9), is obtained by setting $\det[\mathbf{Q}^{(r)}(\omega_1, \omega_2, d_0, \rho^{(r)})] = 0$, which in turn leads to the characteristic equation allowing to evaluate the roots $\rho_I^{(r)}$ $(I = 1, 3)$ by

$$\begin{aligned}&\{(1+C^{(r)})\omega_1^2 + \omega_2^2 - (\rho^{(r)})^2\}\{(k_1^{(r)}\omega_2^2 + k_3^{(r)}\omega_1^2 - k_2^{(r)}(\rho^{(r)})^2)(-k_2^{(r)}\omega_2^2 - k_3^{(r)}\omega_1^2 + k_1^{(r)}(\rho^{(r)})^2 + C^{(r)}C_\perp^{(r)}d_0^2/\varepsilon_0)\\ &\quad -(k_1^{(r)} - k_2^{(r)})^2\omega_2^2(\rho^{(r)})^2\} - \{k_1^{(r)}\omega_2^2 + k_3^{(r)}\omega_1^2 - k_2^{(r)}(\rho^{(r)})^2\}(C^{(r)})^2C_\perp^{(r)}d_0^2\omega_1^2/\varepsilon_0 = 0.\end{aligned} \tag{5.10}$$

For convenience, we have introduced $C^{(r)} \equiv C_\perp^{(r)}/C_b^{(r)}$. The last polynomial is bi-cubic in ρ^2 and thus has six roots $\pm\rho_I^{(r)}(\omega_1, \omega_2, d_0)$, with $I = 1, 2, 3$. Unfortunately, no explicit solution exists for this polynomial in the present case and thus the six roots are obtained numerically.

The remaining $\Delta\widehat{\mathcal{N}}^{I,(r)}$ are then given by simply solving for the first two rows in (5.9), which gives

$$\Delta\widehat{\mathcal{N}}_3^{I,(r)} = -\varepsilon_0\frac{(1+C^{(r)})\omega_1^2 + \omega_2^2 - (\rho_I^{(r)})^2}{C^{(r)}C_\perp^{(r)}d_0\omega_1}, \qquad \Delta\widehat{\mathcal{N}}_2^{I,(r)} = \frac{(k_1^{(r)} - k_2^{(r)})\omega_2\rho_I^{(r)}}{k_2^{(r)}(\rho_I^{(r)})^2 - k_3^{(r)}\omega_1^2 - k_1^{(r)}\omega_2^2}\Delta\widehat{\mathcal{N}}_3^{I,(r)}. \tag{5.11}$$

Finally, the twelve unknown eigenmode amplitudes, denoted in matrix form by $\boldsymbol{\Xi} \equiv [\boldsymbol{\xi}^{c,(1)}, \boldsymbol{\xi}^{s,(1)}, \boldsymbol{\xi}^{c,(2)}, \boldsymbol{\xi}^{s,(2)}]^T$, (with $\boldsymbol{\xi}^{c,(r)} \equiv [\xi_1^{c,(r)}, \xi_2^{c,(r)}, \xi_3^{c,(r)}]^T$ and $\boldsymbol{\xi}^{s,(r)} \equiv [\xi_1^{s,(r)}, \xi_2^{s,(r)}, \xi_3^{s,(r)}]^T$) are determined from the boundary and interface conditions (4.3), (5.2) and (5.6). These conditions lead to a system of twelve homogeneous algebraic equations (see electronic SM) that can be cast in the compact matrix form

$$\mathbf{M}(\omega_1, \omega_2, d_0)\cdot\boldsymbol{\Xi} = \mathbf{0}, \tag{5.12}$$

For a non-trivial solution of $\boldsymbol{\Xi}$, the determinant of $\mathbf{M}$ must vanish. This condition allows us to determine the critical d_0^ω for a given set of $(\omega_1, \omega_2) \in \mathbb{R}^2$. Similar to the numerical study described in Section 4.2, we obtain the critical value of the electric field d_0^c (and the corresponding wavenumbers ω_1^c and ω_2^c) by identifying the minimum of all those d_0^ω attained at different $(\omega_1, \omega_2) \in \mathbb{R}^2$, i.e.,

$$\det[\mathbf{M}(\omega_1, \omega_2, d_0^\omega)] = 0, \qquad d_0^c = \min_{(\omega_1,\omega_2)\in\mathbb{R}^2} d_0^\omega(\omega_1, \omega_2). \tag{5.13}$$

It is worth noting that that ω_1 and ω_2 appear in the characteristic polynomial (5.10) in square powers and thus all four $d_0(\pm\omega_1, \pm\omega_2)$ are equal. Thus, for the zero twist case, it is sufficient to scan only positive ω_1, ω_2. In addition, in all analytical calculations for the LC bilayer, we find $\omega_1^c = 0$, similar to the single layer case (Sfyris et al., 2016).

6. Results

This section presents representative results for the Freedericksz transition in bilayers made of commercially available liquid crystal (LC) materials. Specifically, Table 1 presents the material parameters for six different liquid crystals at room temperature (see Schad et al. (1979), Kelly and O'Neill (2001) and Stewart (2004)). The choice of those materials is somehow arbitrary but reveals a number of new features seen only in the case of bilayer systems.

In all examples considered in this study, we assign the 5CB material to layer $r = 1$ and change the materials used in layer $r = 2$. The volume fraction of layer $r = 2$ is defined as $c \equiv \ell_3^{(2)}/\ell_3$, such that $c = 0$ corresponds to a 5CB single layer.

For convenience in the presentation of the results, we can introduce the dimensionless quantities (Sfyris et al., 2016)

$$x_3/\ell_3 \to x_3, \quad \boldsymbol{\alpha}\sqrt{k_1^{5CB}\varepsilon_0} \to \boldsymbol{\alpha}, \quad \omega_j\ell_3 \to \omega_j, \quad k_i^{(r)}/k_1^{5CB} \to k_i^{(r)}, \quad \zeta \equiv \frac{d_0\,\ell_3}{\varepsilon_0\sqrt{k_1^{5CB}}} = \frac{\Delta\varphi_a}{\sqrt{k_1^{5CB}}}, \tag{6.1}$$

with $j = 1, 2$, $i = 1, 2, 3$, $r = 1, 2$ and k_1^{5CB} given in Table 1. The critical non-dimensional field associated with the critical electric displacement d_0^c is denoted by ζ_c.

Table 1
LC material parameters.

LC	k_1 (pN)	k_2 (pN)	k_3 (pN)	$\chi_\parallel$	$\chi_\perp$	$\Delta\chi = \chi_\parallel - \chi_\perp$
5CB	6.20	3.91	8.2	17.5	6.0	11.5
7E	11.10	5.82	15.97	2.3	3.0	-0.7
PCH7	9.40	7.40	16.3	12.9	4.2	8.5
PCH12	9.41	5.74	24.1	17.2	4.0	13.2
ZLI-2452	15.0	8.40	20.1	8.7	2.6	6.1
MDA-02-2419	8.26	8.26	17.22	40.8	7.25	33.55

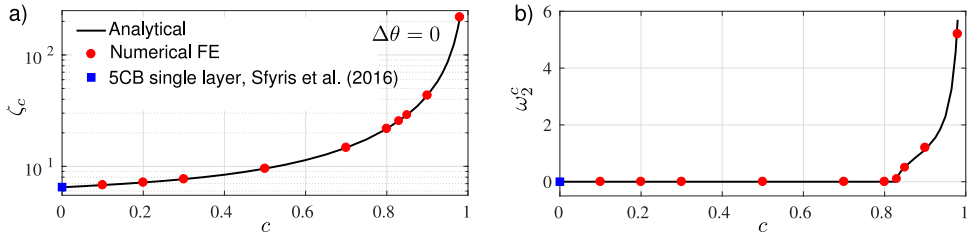

Fig. 4. Bilayer mixing 5CB with 7E. Comparison between the analytical and the numerical FE solutions as a function of the layer volume fraction c for a zero-twist bilayer $\Delta\theta = 0$. (a) The normalized critical electric field $\zeta_c = d_0^c \ell_3 / \sqrt{\varepsilon_0 \, k_1^{5CB}}$ (with $k_1^{5CB} = k_1^{(2)}$ in present notation) and (b) the critical wavenumber ω_2^c. At $c \sim 0.83$ a nonlocal mode $\omega_2^c \neq 0$ emerges.

In the following, the first subsection presents the transition from global (i.e. independent of x_1, x_2 and $\omega_1^c = \omega_2^c = 0$) to local eigenmodes (i.e., $\omega_1^c \neq 0$ and/or $\omega_2^c \neq 0$) as a function of the twist angle $\Delta\theta$ and the volume fraction c in the LC bilayer. The second subsection shows that with properly chosen LC bilayers, one can obtain a critical electric field that is either lower or higher than those achieved in a single layer of the same overall thickness of any of the constituents alone.

6.1. 5CB-7E bilayers and local eigenmodes

Fig. 4 shows (a) the non-dimensional critical electric field ζ_c and (b) the critical wavenumber ω_2^c as a function of the volume fraction c for a zero-twist bilayer ($\Delta\theta = 0$) consisting of 5CB and 7E LCs. For zero twist, we always find $\omega_1^c = 0$. Both Figs. 4a and b show an excellent agreement between the numerical FE and the analytical (for zero-twist) solutions ($< 0.1\%$ error). This validates our numerical analysis, which will subsequently be used to calculate critical electric fields and eigenmodes for the non-zero twist LC bilayers.

In addition to the agreement between the FE and the analytical solutions, one can make two important observations in the context of Fig. 4. In Fig. 4a, we find that $\zeta_c \to \infty$ as $c \to 1$, while in Fig. 4b, we obtain a periodic Freedericksz transition, i.e., a finite wavelength ($\omega_2^c \neq 0$) critical mode for $c > 0.83$. Those two observations are rationalized henceforth.

It is known from the literature (see for instance Stewart (2004)) that the anisotropy of the electric properties, denoted by the anisotropy factor $\Delta\chi = \chi_\parallel - \chi_\perp$ in LC layers controls the critical field ζ_c required for the Freedericksz transition. For $\Delta\chi > 0$, the electric susceptibility $\chi_\parallel$ along the director orientation $\mathbf{n}_0$ is greater than that ($\chi_\perp$) perpendicular to $\mathbf{n}_0$. In this case, the LC molecules tend to rotate from the ground state to the $\widehat{\mathbf{e}}_3$ direction with the application of the applied electric field. Consequently, a competition between the mechanical stiffness of the LC and the dielectric torque due to the applied ζ sets in. Once ζ exceeds a critical value ζ_c, the mechanical stiffness of the LC bulk can no longer sustain the base state orientation of $\mathbf{n}_0$, resulting in the Freedericksz transition (Lonberg and Meyer, 1985; Sfyris et al., 2016). Hence, $\Delta\chi > 0$ is a necessary condition for the Freedericksz transition to take place. The 5CB LC layer exhibits a positive $\Delta\chi^{5CB} = 11.5 > 0$, which explains its ubiquitous application in LCD technology. In contrast, the 7E LC layer has a negative anisotropy factor $\Delta\chi^{7E} = -0.7 < 0$ and thus exhibits no Freedericksz transition. This explains the strong increase of ζ_c with c and ultimately the result of $\zeta_c \to \infty$ as $c \to 1$, in Fig. 4a. We note that for a 5CB single layer (c = 0) the value $\zeta_c \sim 6.5$ matches the corresponding prediction by Sfyris et al. (2016) for a 5CB single layer. The 7E LC layer is *electrically inert* and thus, serves as the electrically passive substrate that is attached to an electrically active 5CB layer.

It is this passive electric response of the 7E material that leads to a non-zero ω_2^c and thus periodic Freedericksz transitions in the x_2 plane for sufficiently large $c > 0.83$, as shown in Fig. 4b. Beyond that volume fraction ω_2^c increases almost exponentially and eventually goes to ∞ as $c \to 1$. Note, on the other hand, that the nematic 5CB single layer ($c = 0$) does not exhibit a periodic Freedericksz transition since $k_1^{5CB}/k_2^{5CB} < 3.3$, which is the minimum value required for such phenomena in single layers (Lonberg and Meyer, 1985). Hence, in the present example, we show that the nonlinear interaction between a thin, electrically active 5CB layer and an electrically passive 7E substrate leads to periodic Freedericksz transition for a untwisted bilayer, even when the k_1/k_2 ratios of both LC materials are less than the critical value $k_1/k_2 = 3.3$.

The observed (finite-wavelength) periodic instability resembles closely the wrinkling instability of a magneto-active elastomer on a non-magnetic substrate (Danas and Triantafyllidis, 2014; Psarra et al., 2017). The essential difference of the present case with the magnetic film-substrate instability is the strong anchoring at both ends, which is not present in the

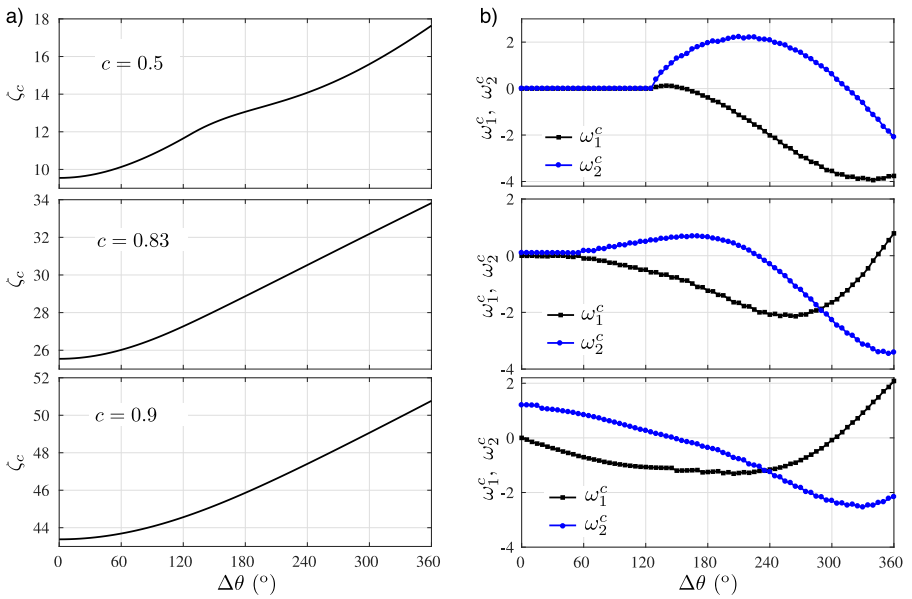

Fig. 5. (a) Normalized critical field ζ_c and (b) corresponding critical wavenumbers ω_1 and ω_2 as a function of the total twist angle $\Delta\theta$ for bilayers of 5CB and 7E with volume fractions $c = 0.5, 0.83, 0.9$. At $c = 0.83$, ω_2 becomes non-zero for $\Delta\theta = 0$ and increases further for $c = 0.9$.

latter. The spontaneous periodic patterning of a free-standing 5CB thin layer (i.e. no anchoring) resting on a soft polymer (or a liquid substrate) has been observed experimentally in Lavrentovich and Pergamenshchik (1990). In those cases, the surface tension of the thin 5CB layer becomes a critical factor for such a periodic instability pattern. On the other hand, the present work demonstrates that even in the case of strong anchoring conditions, a nematic (untwisted) 5CB thin layer resting on an electrically passive 7E substrate can undergo a periodic Freedericksz transition (with $\omega_2^c \neq 0$).

Next, we explore the effect of the twist angle $\Delta\theta > 0$. Fig. 5a shows the evolution of the critical non-dimensional electric field ζ_c as a function of $\Delta\theta$ for three volume fractions $c = 0.5, 0.83, 0.9$. The corresponding critical wavenumbers are shown in Fig. 5b. We observe in Fig. 5a that increase of the twist angle $\Delta\theta$ leads to the increase of ζ_c. This observation is in qualitative agreement with the analytical results of Leslie (1970) for 2D LC single layers. In that study, the critical field is found to be related to the twist angle by $\zeta_c \sim \sqrt{\pi^2 k_1 + (k_3 - 2k_2)\Delta\theta^2}$. This relation was later validated experimentally by Karat and Madhusudana (1977). The factor $(k_3 - 2k_2)$ plays a key role since it *roughly* indicates the slope of ζ_c as a function of $\Delta\theta$. In particular, we notice from Table 1 that for both 5CB and 7E, $(k_3 - 2k_2) > 0$, which implies an increasing ζ_c with $\Delta\theta$ and is indeed observed in the 3D numerical FE computations in Fig. 5a. In turn, if k_3 is sufficiently small with respect to k_2 one can get a decrease of ζ_c, as already discussed in Sfyris et al. (2016).

Fig. 5b shows in more detail the passage from a simple splay (i.e. global) Freedericksz transitions (i.e., $\omega_1 = \omega_2 = 0$) to periodic Freedericksz patterning as a function of the twist angle $\Delta\theta$. Specifically, twisted 5CB single layers ($c = 0$) are found to exhibit a periodic critical mode with $\omega_1^c, \omega_2^c \neq 0$ beyond a certain $\Delta\theta > 120^o$ (Scheffer and Nehring, 1997; Sfyris et al., 2016).

In turn, in the context of 5CB-7E bilayers, the critical twist angle $\Delta\theta$ at which ω_2 becomes non-zero decreases with increase of c (i.e., increase of 7E volume fraction). Eventually, at $c \sim 0.83$, the LC bilayer exhibits a very small but non-zero ω_2 for $\Delta\theta = 0$. The ω_1^c always remains zero for $\Delta\theta = 0$ as discussed earlier. The corresponding critical wavenumbers ω_1^c and ω_2^c are then found to vary with $\Delta\theta$ after that threshold value is reached as a function of the volume fraction c. In particular, ω_1^c and ω_2^c exhibit a highly non-monotonic dependence on $\Delta\theta$. Hence, a pure splay pattern can never be achieved once we go beyond a critical twist angle $\Delta\theta$ which leads to periodic Freedericksz transitions.

In Fig. 6a, we collectively plot the critical electric field ζ_c in the $c - \Delta\theta$ space, where we observe a monotonic increase of ζ_c with respect to both c and $\Delta\theta$, while Fig. 6b,c show the corresponding ω_1^c and ω_2^c in the same $c - \Delta\theta$ space. The thick red lines in both Figs. 6b and c indicate the transition between the splay (global) and periodic (local) critical modes. It is noted that the separating line between splay (global) and periodic (local) eigenmodes remains at $\Delta\theta \sim 120^o$ up to a volume fraction of $c = 0.7$. Then, a rapid decrease in this transition angle of twist $\Delta\theta$ is obtained between $0.7 < c < 0.83$, after which periodic critical modes $\omega_1^c, \omega_2^c \neq 0$ are found for all possible twist angles.

In Figs. 7 and 8, we plot a series of eigenmodes associated with some of the above described critical electric fields, twist angles and volume fractions for the 5CB-7E LC bilayer. Specifically, Fig. 7 shows the critical modes of a 5CB-7E bilayer with $c = 0.5$ under three different twist angles $\Delta\theta = 270^o$ and 360^o. The patterns are depicted in a $[1 \times 1 \times 1]$ representative volume element of the bilayer with thickness $\ell_3 = 1$.

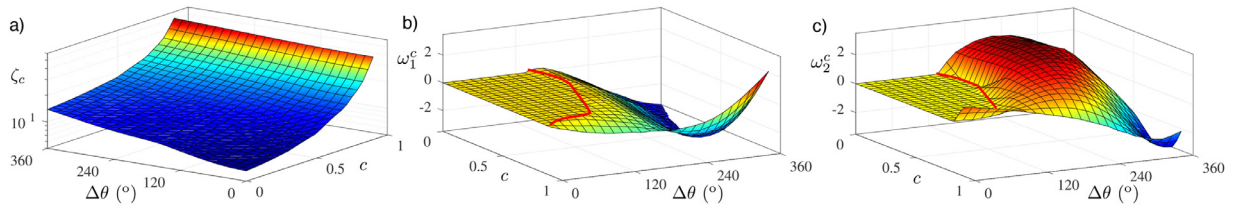

Fig. 6. Stability results as functions of volume fraction and applied twist angle for a 5CB – 7E bilayer. (a) Normalized critical field ζ_c and corresponding critical wavenumbers (b) ω_1 and (c) ω_2 as a function of the total twist angle $\Delta\theta$ and the bilayer volume fraction c. The red continuous line in (b) and (c) defines the boundary beyond which the corresponding eigenmode is nonlocal (periodic Freedericksz transition, $\omega_1^c \neq \omega_2^c \neq 0$). (For interpretation of the references to colour in this figure legend, the reader is referred to the web version of this article.)

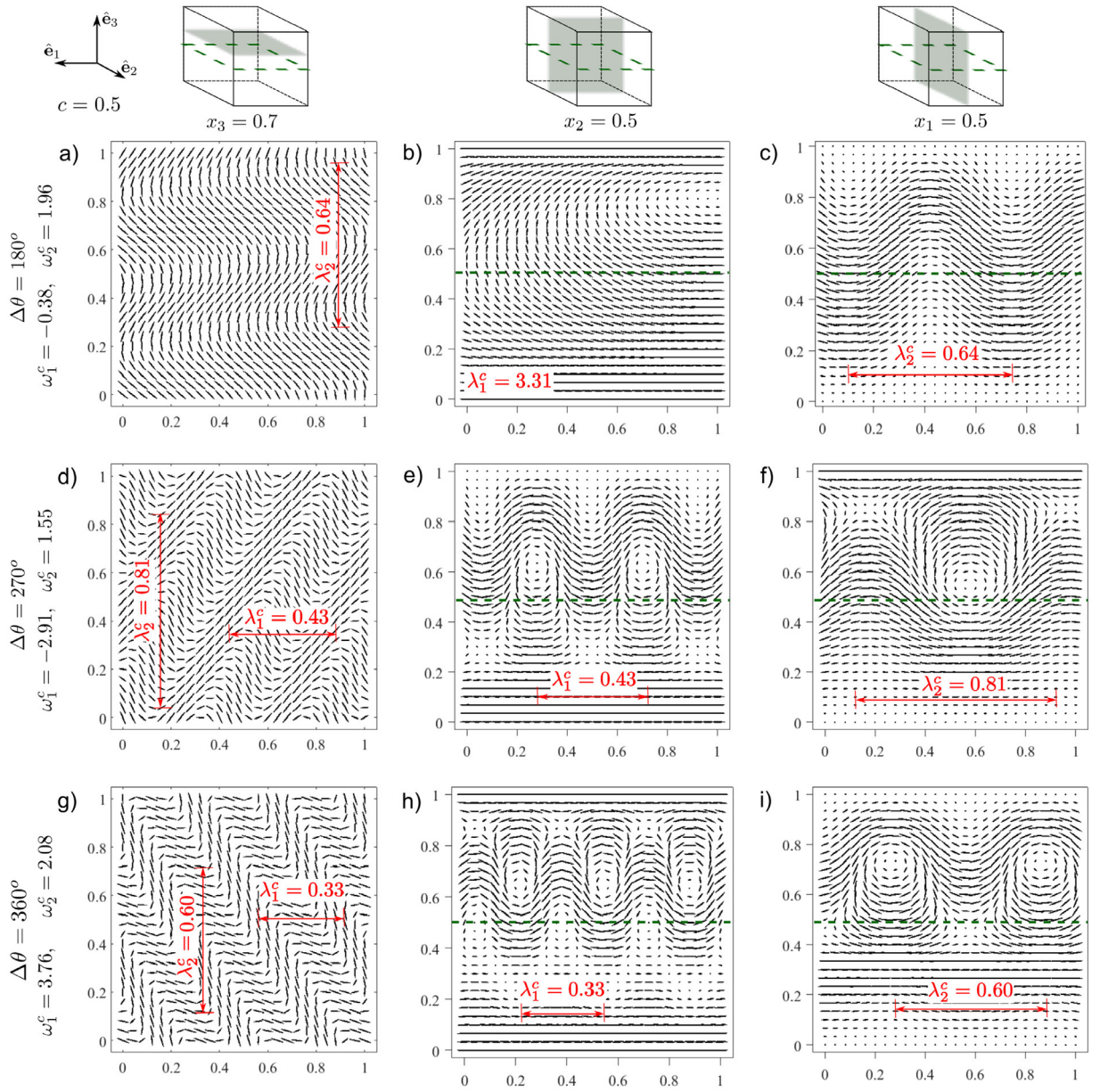

Fig. 7. Projections of the post-bifurcated director field **n** exhibiting periodic (local) Freedericksz transitions patterns. Different cross-sections of a 5CB-7E bilayer with $c = 0.5$ under different twist angles $\Delta\theta$ are shown. (a)-(c) $\Delta\theta = 180^o$, (d)-(f) $\Delta\theta = 270^o$ and (g)-(i) $\Delta\theta = 360^o$.

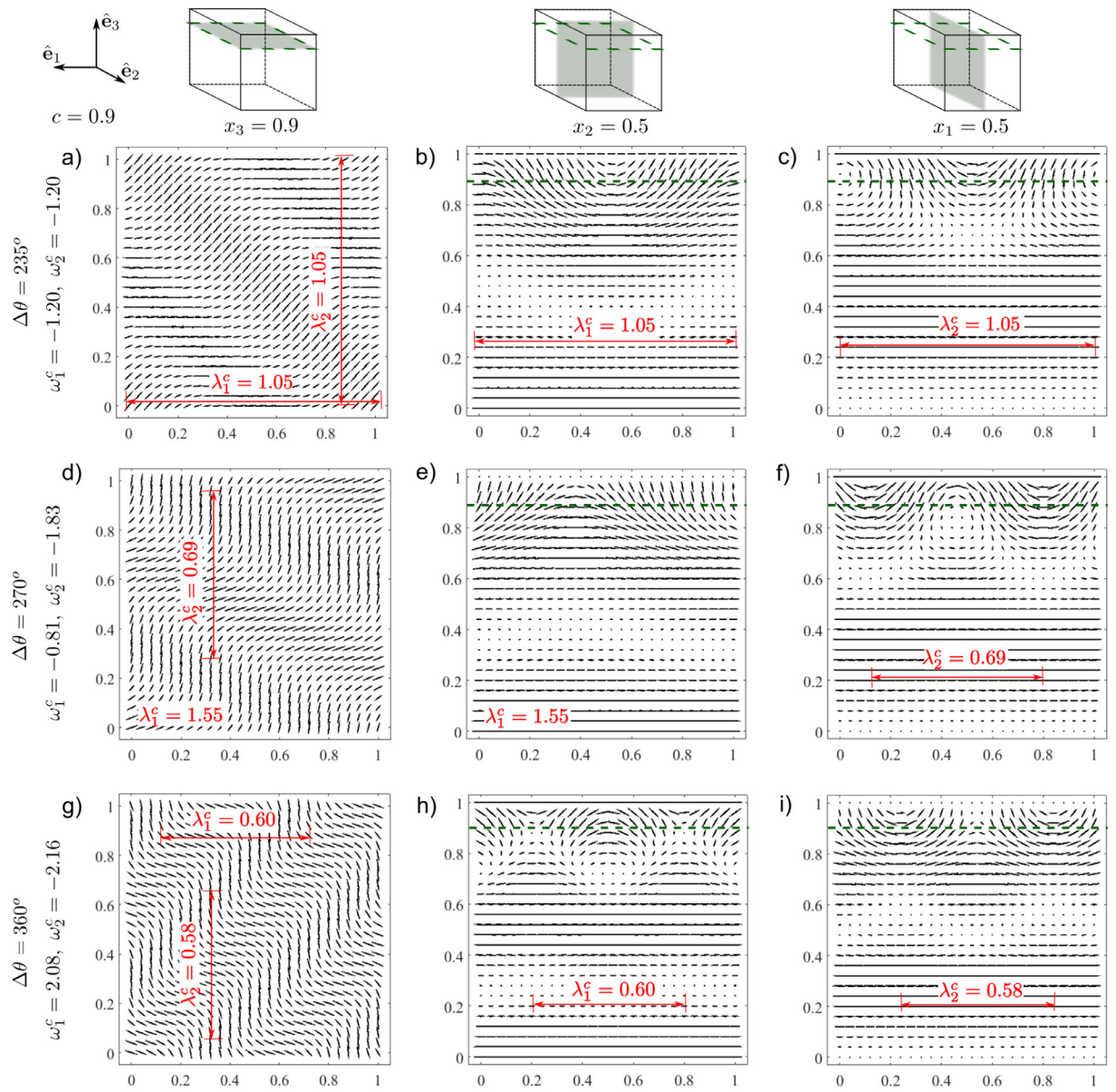

Fig. 8. Projections of the post-bifurcated director field $\mathbf{n}$ exhibiting periodic (local) Freedericksz transitions patterns. Different cross-sections of a 5CB-7E bilayer with $c = 0.9$ under different twist angles $\Delta\theta$ are shown. (a)-(c) $\Delta\theta = 235^o$, (d)-(f) $\Delta\theta = 270^o$ and (g)-(i) $\Delta\theta = 360^o$.

In particular, for each $\Delta\theta$, we depict three different cross-sections of the LC bilayer, which are parallel to the three Cartesian coordinate axes. Therein, we plot projections of the post-bifurcated director field, $\mathbf{n}(\mathbf{x}) = \mathbf{n}_0(\mathbf{x}) + q\,\Delta\mathbf{n}$ with $\mathbf{n}_0$ given by (3.15) and $\Delta\mathbf{n}$ being the computed critical eigenmode at bifurcation. The amplification factor q is used only for visualization purposes. The vertical sections $x_2 = 0.5$ and $x_1 = 0.5$ show one dimensional waves with wavelengths λ_1 and λ_2, respectively. A greater tilt (i.e., inclination with the $1-2$ plane) of LC molecules is observed in the 5CB layer as compared to the 7E layer because of the higher Franck-Oseen (FO) constants of the 7E layer. Thus, the maximum tilt is obtained near $c \sim 0.65$, which is well above the interface. On the other hand, the horizontal sections at $x_3 = 0.7$ display two dimensional *striped patterns*, which are also observed experimentally for TNDs (Chigrinov et al., 1979; Scheffer and Nehring, 1997). These patterns are the result of the superposition of two waves along $\hat{\mathbf{e}}_1$ and $\hat{\mathbf{e}}_2$. The striped patterns depend on the magnitudes of ω_1^c and ω_2^c. A lower $|\omega_1^c|$ or $|\omega_2^c|$ results in strip patterns parallel to $\hat{\mathbf{e}}_1$ or $\hat{\mathbf{e}}_2$, respectively. For example, Fig. 7a shows that a critical wavenumber $\omega_1^c = -0.38$ results in a *nearly* horizontal strip pattern with wavelength λ_2^c. Strip patterns with a positive inclination to $\hat{\mathbf{e}}_1$ are observed when the signs of ω_1^c and ω_2^c are of opposite sign (see e.g., Fig. 7d). On the other hand, negatively inclined strips to $\hat{\mathbf{e}}_1$ are observed when the signs of ω_1^c and ω_2^c are the same (see Fig. 7g).

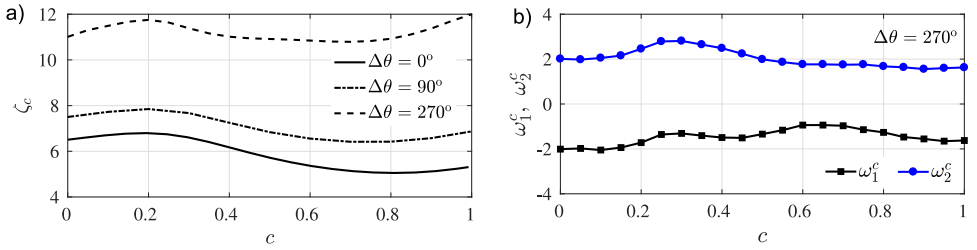

Fig. 9. 5CB-PCH12 LC bilayer results. (a) Critical non-dimensional electric field ζ_c for three twist angles $\Delta\theta = 0, 90, 270^o$ and (b) critical wavenumbers for a twist angle $\Delta\theta = 270^o$ as functions of the bilayer volume fraction c.

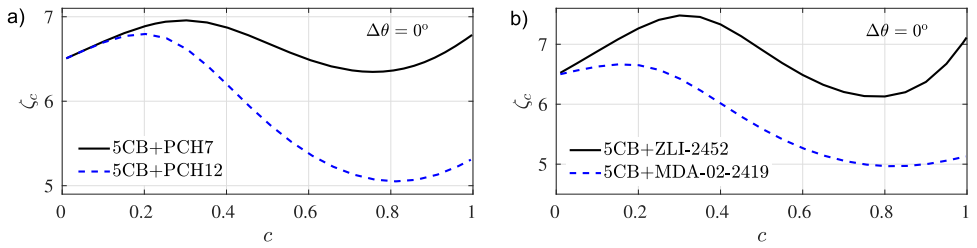

Fig. 10. Critical non-dimensional electric field ζ_c as a function of the bilayer volume fraction c for twist angles $\Delta\theta = 0$. Assembly of (a) 5CB-PCH7 and 5CB=PCH12 and (b) 5CB-ZLI-2452 and 5CB-MDA-02-2419 bilayers.

Critical modes for $c = 0.9$ bilayers, subjected to three different twists $\Delta\theta = 235^o, 270^o$ and 360^o are depicted in Fig. 8. Unlike Fig. 7, the bulk patterns are less pronounced in Fig. 8 due to a larger volume fraction of the mechanically stiffer 7E phase. Considerable periodic undulations are observed only near the interface and in the thin 5CB layer (see Figs. 8b, c, e, f, h and i). The $x_3 = 0.9$ sections (8 a, d and g) show strip patterns with various widths and inclinations depending on ω_1^c and ω_2^c. The amplitude of these strip patterns is maximum in the soft 5CB layer and vanishes gradually below the interface.

6.2. Non-monotonic critical fields in bilayers

In this section, we present a novel and interesting feature obtained in LC bilayers consisting of phases that have relatively similar dielectric properties but different mechanical properties. Specifically, in the following calculations we will use 5CB as the base phase combined with PCH7, PCH12, ZLI-22452 and MDA-02-2419 materials, as defined in Table 1. Contrary to the previous sections, all materials used here exhibit a strong dielectric anisotropy with similar values for their dielectric permeability in most cases, whereby some of the mechanical constants of 5CB are even less than half of those of the other LC materials.

In Fig. 9, we investigate a 5CB-PCH12 bilayer for three twist angles $\Delta\theta = 0, 90, 270^o$ as a function of the bilayer volume fraction. The main observation in the context of this figure is the striking non-monotonicity of the critical non-dimensional electric field ζ_c as a function of c. Specifically, in Fig. 9a, the two extreme cases $c = 0$ (single layer 5CB) and $c = 1$ (single layer PCH12) exhibit similar values of ζ_c. By mixing the two, however, one gets critical fields, ζ_c, that can be higher (e.g. for $c = 0.2$) or even lower (e.g. for $c = 0.8$) than any of the two single layer LCs. Furthermore, this non-monotonic feature is not affected qualitatively by the twist angle $\Delta\theta$, but rather leads to a simple shift of the curves upwards. In turn, in Fig. 9b, we observe that $\omega_1^c = \omega_2^c = 0$ (not shown) except for $\Delta\theta = 270^o$ in which case they are finite and remain fairly insensitive to the volume fraction c.

Finally, in Fig. 10, we show several combinations of various bilayers for twist angles $\Delta\theta = 0$. Perhaps the most interesting observation that can be made in the context of this figure is that the maximum effect of non-monotonicity is observed for bilayers made of constituents that exhibit fairly similar critical ζ_c in their single layer state, such as the 5CB-PCH7 and 5CB-ZLI-2452 cases. These observations may have interesting implications for current LC technology, since a bilayer LC device of two LCs with given Freedericksz transition thresholds can be lower and thus energetically more desirable than any of the two LC single layer devices.

7. Concluding remarks

In this work, we present a theoretical investigation of an assembly of two different liquid crystal (LC) materials in a bilayer geometry, which is subjected to a transverse (i.e., normal to the bilayer interface) electric field. We then carry out a fully three-dimensional analysis of the Freedericksz transition phenomenon using two equivalent variational formulations under strongly anchored boundary conditions for the director field **n**. First, we introduce a reduced potential energy allowing to obtain the ground state of the director field in the LC bilayer. Subsequently, we perform a combined analytical-numerical

one-dimensional bifurcation analysis along the bilayer thickness for arbitrary twist angles and volume fractions of the two phases constituting the LC bilayer. This is achieved by use of an electric vector potential minimum variational principle leading to a global minimization of the LC energy. We also use a scalar electric potential variational formulation to obtain an analytical solution for the Freedericksz transition in bilayers with zero twist angle. The two approaches are shown to coincide for this latter case.

One of the key results of the present study consists in showing that a LC bilayer made of a 5CB and 7E materials can exhibit periodic Freedericksz transitions (i.e. local bifurcation modes with finite wavenumbers) for zero twist angles, even if none of the constituents alone leads to such local modes (Sfyris et al., 2016). In fact, this can be achieved by assembling a relatively thin electrically active LC such as the 5CB together with an electrically inert (i.e. passive) LC such as the 7E. In that case, and for zero twist angle, we show that by increasing the volume fraction of 7E (i.e. making the 5CB layer thinner) at a given value of the volume fraction $c \sim 0.83$, we obtain a periodic Freedericksz transition in one of the two in-plane directions. If we apply the electric field along the direction $\mathbf{e}_3$ and the LC director vector for zero twist is along direction $\mathbf{e}_1$, the periodic Freedericksz transition appears along direction $\mathbf{e}_2$. This feature persists as the twist angle increases but now leads to complex periodic patterns along both in plane directions, i.e. non-zero wavenumbers along $\mathbf{e}_1$ and $\mathbf{e}_2$. At the same time, the corresponding critical electric field needed to trigger this periodic bifurcation strongly increases going finally to infinity since the 7E LC does not show any Freedericksz transition for finite electric fields. This response is somewhat analogous to the problem of wrinkling observed in mechanical film/substrate (Audoly and Boudaoud, 2008) or magnetorheological (Danas and Triantafyllidis, 2014; Psarra et al., 2017) or dielectric (Wang and Zhao, 2013) film/substrate systems.

The second novel observation of the present study is the resulting non-monotonicity of the critical electric field as a function of the bilayer volume fraction when the two assembled materials exhibit similar dielectric properties but different mechanical ones. In particular, individual 5CB and PCH single layers exhibit long-wave Freedericksz transitions at fairly similar critical electric fields. If, however, they are put together in a bilayer geometry, the resulting critical electric field can be higher or even lower than that corresponding to the individual single layers alone. This non-monotonic dependence on the volume fraction of the phases in LC bilayers reveals at one hand the highly nonlinear and non-intuitive character of the Freedericksz transition and on the other hand the possibility of designing novel more energy efficient LC multi-layer devices. In particular, one can generalize the present study to *N*-layer or even more complex nano and microstructured LC geometries in a straightforward manner. The experimental feasibility of such LC devices remains, in turn, an open question. It should be, however, possible to obtain such systems using liquid crystal elastomeric films (Hauser et al., 2016).

In closing, we note that in the present study we consider strongly anchoring conditions. In general, it is possible to consider more complex boundary conditions, such as weak anchoring, but in some cases, this might require a fully three dimensional FE resolution of the problem at hand. Furthermore, it is well known that LCs may contain defects that can change significantly the observed patterns especially when they exhibit periodic Freedericksz transitions. In addition, these patterns can gradually change and even exhibit secondary bifurcations at higher electric fields. In this sense, the present study presents bifurcation eigenmodes, but the post-bifurcated solutions and their stability are still an open question in three-dimensions and multi-layer systems. In general such calculations, will require a fully three-dimensional numerical solution. Such a work is in progress.

Acknowledgments

KD, DM and KH wish to acknowledge support from the European Research Council (ERC) under the European Unions Horizon 2020 research and innovation program (Grant agreement no. 636903-MAGNETO). NT acknowledges support from the Foundation of the Ecole Polyechnique for his work on Liquid Crystals.

Supplementary materials

Supplementary material associated with this article can be found, in the online version, at doi:10.1016/j.jmps.2018.09.008.

References

Agrawal, A., Yun, T., Pesek, S.L., Chapman, W.G., Verduzco, R., 2014. Shape-responsive liquid crystal elastomer bilayers. Soft Matter 10 (9), 1411–1415. doi:10.1039/c3sm51654g.

Alexe-Ionescu, A.L., Barbero, G., Lelidis, I., 2002. Periodic deformations in nematic liquid crystals. Phys. Rev. E 66 (6). doi:10.1103/physreve.66.061705.

Atherton, T.J., Sambles, J.R., 2006. Orientational transition in a nematic liquid crystal at a patterned surface. Phys. Rev. E 74 (2). doi:10.1103/physreve.74.022701.

Audoly, B., Boudaoud, A., 2008. Buckling of a stiff film bound to a compliant substrate–part i:: formulation, linear stability of cylindrical patterns, secondary bifurcations. J. Mech. Phys. Solids 56 (7), 2401–2421. doi:10.1016/j.jmps.2008.03.003.

Barbero, G., Durand, G., 1987. On a possible mechanism for the spontaneous freedericksz effect. Liq. Cryst. 2 (3), 401–403. doi:10.1080/02678298708086685.

Bíró, O., Preis, K., 1984. On the use of the magnetic vector potential in the finite element analysis of three-dimensional eddy currents. IEEE Trans. Magn. 25 (4), 3145.

Bladon, P., Terentjev, E., Warner, M., 1993. Transitions and instabilities in liquid crystal elastomers. Phys. Rev. E 47 (6), R3838.

Blinov, L., 1979. Domain instabilities in liquid crystals. Le Journal de Physique Colloques 40 (C3), C3–247.

Boothby, J.M., Ware, T.H., 2017. Dual-responsive, shape-switching bilayers enabled by liquid crystal elastomers. Soft Matter 13 (24), 4349–4356. doi:10.1039/c7sm00541e.

Bustamante, R., Dorfmann, A., Ogden, R.W., 2009. Nonlinear electroelastostatics: a variational framework. Zeitschrift für angewandte Mathematik und Physik 60 (1), 154–177.

Chigrinov, V.G., Belyaev, V.V., Belyaev, S.V., Grebenkin, M.F., 1979. Instability of cholesteric liquid crystals in an electric field. Soviet J. Exp. Theor.Phys. 50, 994.
Danas, K., 2017. Effective response of classical, auxetic and chiral magnetoelastic materials by use of a new variational principle. J. Mech. Phys. Solids 105, 25–53.
Danas, K., Triantafyllidis, N., 2014. Instability of a magnetoelastic layer resting on a non-magnetic substrate. J. Mech. Phys. Solids 69, 67–83. doi:10.1016/j.jmps.2014.04.003.
Ericksen, J., 1962. Nilpotent energies in liquid crystal theory. Arch. Ration. Mech. Anal. 10 (1), 189–196.
Frank, F.C., 1958. I. liquid crystals. on the theory of liquid crystals. Discuss Faraday Soc. 25, 19–28.
Fréedericksz, V., Repiewa, A., 1927. Theoretisches und experimentelles zur frage nach der natur der anisotropen flüssigkeiten. Zeitschrift für Physik A Hadrons and Nuclei 42 (7), 532–546.
Gerritsma, C., de Jeu, W., Zanten, P.V., 1971. Distortion of a twisted nematic liquid crystal by a magnetic field. Phys. Lett. A 36 (5), 389–390. doi:10.1016/0375-9601(71)90273-8.
Gray, G.W., Kelly, S.M., 1999. Liquid crystals for twisted nematic display devices. J. Mater. Chem. 9 (9), 2037–2050. doi:10.1039/a902682g.
Hauser, A.W., Liu, D., Bryson, K.C., Hayward, R.C., Broer, D.J., 2016. Reconfiguring nanocomposite liquid crystal polymer films with visible light. Macromolecules 49 (5), 1575–1581. doi:10.1021/acs.macromol.6b00165.
Karat, P.P., Madhusudana, N.V., 1977. Verification of leslie's expression for the threshold field of a twisted nematic cell. Mol. Cryst. Liq. Cryst. 40 (1), 171–175. doi:10.1080/15421407708084480.
Kaznacheev, A., Sonin, A., 1983. Mechanism of spontaneous fredericks effect.
Keip, M.-A., Rambausek, M., 2017. Computational and analytical investigations of shape effects in the experimental characterization of magnetorheological elastomers. Int. J. Solids Struct. 121, 1–20. doi:10.1016/j.ijsolstr.2017.04.012.
Kelly, S., O'Neill, M., 2001. Liquid crystals for electro-optic applications. In: Handbook of Advanced Electronic and Photonic Materials and Devices. Elsevier, pp. 1–66. doi:10.1016/b978-012513745-4/50057-3.
Kini, U., 1987. Magnetic field induced generalized freedericksz transition in a rigidly anchored simple twisted nematic. J. Phys. 48 (7), 1187–1196. doi:10.1051/jphys:019870048070118700.
Kirsch, P., Bremer, M., 2000. Nematic liquid crystals for active matrix displays: molecular design and synthesis. Angewandte Chemie 39 (23), 4216–4235. doi:10.1002/1521-3773(20001201)39:23<4216::aid-anie4216)3.0.co;2-k.
Lavrentovich, O.D., Pergamenshchik, V.M., 1990. Periodic domain structures in thin hybrid nematic layers. Mol. Cryst. Liq. Cryst.Incorporating Nonlinear Opt. 179 (1), 125–132. doi:10.1080/00268949008055362.
Lavrentovich, O.D., Pergamenshchik, V.M., 1996. Patterns in thin liquid crystal films and the divergence (sufacelike) elasticity. In: Liquid Crystals in the Nineties and Beyond. World Scientific, pp. 251–299. doi:10.1142/9789812831101_0008.
Lefèvre, V., Danas, K., Lopez-Pamies, O., 2017. A general result for the magnetoelastic response of isotropic suspensions of iron and ferrofluid particles in rubber, with applications to spherical and cylindrical specimens. J. Mech. Phys. Solids 107, 343–364. doi:10.1016/j.jmps.2017.06.017.
Leslie, F.M., 1968. Some constitutive equations for liquid crystals. Arch. Ration. Mech. Anal. 28 (4), 265–283.
Leslie, F.M., 1970. Distortion of twisted orientation patterns in liquid crystals by magnetic fields. Mol. Cryst. Liq. Cryst. 12 (1), 57–72. doi:10.1080/15421407008082760.
Liu, D., Liu, L., Onck, P.R., Broer, D.J., 2015. Reverse switching of surface roughness in a self-organized polydomain liquid crystal coating. Proc. Natl. Acad. Sci. 112 (13), 3880–3885.
Liu, Q., Zhan, Y., Wei, J., Ji, W., Hu, W., Yu, Y., 2017. Dual-responsive deformation of a crosslinked liquid crystal polymer film with complex molecular alignment. Soft Matter 13 (36), 6145–6151. doi:10.1039/c7sm01291h.
Lonberg, F., Meyer, R.B., 1985. New ground state for the splay-fréedericksz transition in a polymer nematic liquid crystal. Phys. Rev. Lett. 55 (7), 718.
Oseen, C., 1933. The theory of liquid crystals. Trans. Faraday Soc. 29 (140), 883–899.
Pampolini, G., Triantafyllidis, N., 2018. Continuum electromechanical theory for nematic continua with application to freedericksz instability. J. Elast. 132 (2), 219–242. doi:10.1007/s10659-017-9665-y.
Psarra, E., Bodelot, L., Danas, K., 2017. Two-field surface pattern control via marginally stable magnetorheological elastomers. Soft Matter 13 (37), 6576–6584. doi:10.1039/c7sm00996h.
Rosso, R., Virga, E.G., Kralj, S., 2004. Local elastic stability for nematic liquid crystals. Phys. Rev. E 70 (1). doi:10.1103/physreve.70.011710.
Schad, H., Baur, G., Meier, G., 1979. Elastic constants and diamagnetic anisotropy of p-disubstituted phenylcyclohexanes (PCH). J. Chem. Phys. 70 (6), 2770–2774. doi:10.1063/1.437862.
Schadt, M., Helfrich, W., 1971. Voltage-dependent optical activity of a twisted nematic liquid crystal. Appl. Phys. Lett. 18 (4), 127–128.
Scheffer, T., Nehring, J., 1997. Supertwisted nematic (stn) liquid crytal displays. Annu. Rev. Mater. Sci. 27 (1), 555–583. doi:10.1146/annurev.matsci.27.1.555.
Sfyris, G., Danas, K., Wen, G., Triantafyllidis, N., 2016. Freedericksz instability for the twisted nematic device: a three-dimensional analysis. Phys. Rev. E 94 (1), 012704.
Sonnet, A.M., Virga, E.G., 2017. Bistable curvature potential at hyperbolic points of nematic shells. Soft Matter 13 (38), 6792–6802.
Sparavigna, A., Lavrentovich, O.D., Strigazzi, A., 1994. Periodic stripe domains and hybrid-alignment regime in nematic liquid crystals: threshold analysis. Phys. Rev. E 49 (2), 1344–1352. doi:10.1103/physreve.49.1344.
Sprang, H.A.V., Aartsen, R.G., 1985. Torsional anchoring of 5cb and 5pch on various substratest. Mol. Cryst. Liq. Cryst. 123 (1), 355–368. doi:10.1080/00268948508074790.
Stark, S., Semenov, A.S., Balke, H., 2015. On the boundary conditions for the vector potential formulation in electrostatics. Int. J. Numer. Methods Eng. 102 (11), 1704–1732. doi:10.1002/nme.4859.
Stewart, I.W., 2004. The Static and Dynamic Continuum Theory of Liquid Crystals: AMathematical Introduction. Crc Press.
Sugimura, A., Luckhurst, G.R., Zhong-can, O.-Y., 1995. Director deformation of a twisted chiral nematic liquid crystal cell with weak anchoring boundaries. Phys. Rev. E 52 (1), 681–689. doi:10.1103/physreve.52.681.
Sugimura, A., Miyamoto, T., Tsuji, M., Kuze, M., 1998. Determination of the unified surface-anchoring energy of a nematic liquid crystal on a polymer substrate. Appl. Phys. Lett. 72 (3), 329–331. doi:10.1063/1.120727.
Virga, E., 1994. Variational Theories for Liquid Crystals. Applied Mathematics and Mathematical Computation.
Wang, Q., Zhao, X., 2013. Creasing-wrinkling transition in elastomer films under electric fields. Phys. Rev. E 88, 042403. doi:10.1103/PhysRevE.88.042403.
Warner, M., Terentjev, E.M., 2003. Liquid Crystal Elastomers, 120. OUP Oxford.
Wysocki, J., Adams, J., Haas, W., 1969. Electric-field induced phase change in cholesteric liquid crystals. Mol. Cryst. 8 (1), 471–487. doi:10.1080/15421406908084922.